



HAL
open science

Pre-encounter Predictions of DART Impact Ejecta Behavior and Observability

Eugene G Fahnestock, Andrew F Cheng, Stavro Ivanovski, Patrick Michel, Sabina D Raducan, Alessandro Rossi, Paul A Abell, Steven Chesley, Elisabetta Dotto, Fabio Ferrari, et al.

► **To cite this version:**

Eugene G Fahnestock, Andrew F Cheng, Stavro Ivanovski, Patrick Michel, Sabina D Raducan, et al.. Pre-encounter Predictions of DART Impact Ejecta Behavior and Observability. *The Planetary Science Journal*, 2022, 3 (9), 10.3847/psj/ac7fa1 . hal-03835348

HAL Id: hal-03835348

<https://hal.science/hal-03835348>

Submitted on 31 Oct 2022

HAL is a multi-disciplinary open access archive for the deposit and dissemination of scientific research documents, whether they are published or not. The documents may come from teaching and research institutions in France or abroad, or from public or private research centers.

L'archive ouverte pluridisciplinaire **HAL**, est destinée au dépôt et à la diffusion de documents scientifiques de niveau recherche, publiés ou non, émanant des établissements d'enseignement et de recherche français ou étrangers, des laboratoires publics ou privés.



Pre-encounter Predictions of DART Impact Ejecta Behavior and Observability

Eugene G. Fahnestock¹, Andrew F. Cheng², Stavro Ivanovski³, Patrick Michel⁴, Sabina D. Raducan⁵, Alessandro Rossi⁶, Paul A. Abell⁷, Steven Chesley¹, Elisabetta Dotto⁸, Fabio Ferrari⁵, Ludmilla Kolokolova⁹, Emily Kramer¹, Jian-Yang Li¹⁰, Stephen R. Schwartz^{11,12}, Stefania Soldini¹³, Gonzalo Tancredi¹⁴, Adriano Campo Bagatin¹⁵, and Yun Zhang⁴

¹ Jet Propulsion Laboratory, California Institute of Technology, Pasadena, CA 91109, USA; Eugene.G.Fahnestock@jpl.nasa.gov

² Johns Hopkins University Applied Physics Laboratory, Laurel, MD 20723, USA

³ INAF–Osservatorio Astronomico di Trieste, Trieste I-34143, Italy

⁴ Université Côte d’Azur, Observatoire de la Côte d’Azur, CNRS, Laboratoire Lagrange, Nice F-06304, France

⁵ Space Research and Planetary Sciences, Physics Institute, University of Bern, Bern, 3012, Switzerland

⁶ IFAC-CNR, Sesto Fiorentino I-50019, Italy

⁷ NASA Johnson Space Center, Houston, TX 77058, USA

⁸ INAF–Osservatorio Astronomico di Roma, Rome, I-00078, Italy

⁹ Department of Astronomy, University of Maryland, College Park, MD 20742, USA

¹⁰ Planetary Science Institute, Fairfax, VA 22030, USA

¹¹ Planetary Science Institute, Tucson, AZ 85719, USA

¹² Lunar & Planetary Laboratory, University of Arizona, Tucson, AZ 85721, USA

¹³ Department of Mechanical, Materials and Aerospace Engineering, University of Liverpool, Liverpool, L69 3GH, UK

¹⁴ Departamento de Astronomía, Facultad de Ciencias, Udelar, Iguá 4225, 11400 Montevideo, Uruguay

¹⁵ IUFACyT–DFISTS, Universidad de Alicante, P.O. Box E-99-03080 Alicante, Spain

Received 2022 February 1; revised 2022 July 1; accepted 2022 July 6; published 2022 September 1

Abstract

We overview various efforts within the DART Investigation Team’s Ejecta Working Group to predict the characteristics, quantity, dynamical behavior, and observability of DART impact ejecta. We discuss various methodologies for simulation of the impact/cratering process with their advantages and drawbacks in relation to initializing ejecta for subsequent dynamical propagation through and away from the Didymos system. We discuss the most relevant forces acting on ejecta once decoupled from Dimorphos’s surface and highlight various software packages we have developed and used to dynamically simulate ejecta under the action of those forces. With some additional software packages, we explore the influence of additional perturbing effects, such as interparticle collisions within true N -body codes and nonspherical and rotating particles’ interplay with solar radiation pressure. We find that early-timescale and close-proximity ejecta evolution is highly sensitive to some of these effects (e.g., collisions) while relatively insensitive to other factors. We present a methodology for turning the time-evolving size- and spatially discretized number density field output from ejecta simulations into synthetic images for multiple platforms/cameras over wide-ranging vantage points and timescales. We present such simulated images and apply preliminary analyses to them for nominal and off-nominal cases bracketing realistic total mass of ejecta and ejecta cumulative size–frequency distribution slope. Our analyses foreshadow the information content we may be able to extract from the actual images taken during and after the DART encounter by both LICIACube and Earth-vicinity telescopes.

Unified Astronomy Thesaurus concepts: [Impact phenomena \(779\)](#); [Asteroids \(72\)](#); [Near-Earth objects \(1092\)](#); [Planetary science \(1255\)](#); [Ejecta \(453\)](#); [N-body simulations \(1083\)](#); [Astronomical simulations \(1857\)](#)

1. Introduction

The Double Asteroid Redirection Test (DART) is a NASA mission that will be the first meaningful demonstration of the use of a kinetic impactor for defense against objects on a collision course with our planet (Cheng et al. 2016, 2018; Rivkin et al. 2021). Having successfully launched on 2021 November 24, the spacecraft will impact (65803) Didymos I Dimorphos, the satellite of the (65803) Didymos binary system, on 2022 September 26 at approximately 23:14 UTC, causing a minimum 73 s change in the binary mutual orbit period that will be measurable from the ground. The actual impact-induced change in this period will be determined by the momentum of the spacecraft and the fate of any resulting ejecta. The

momentum transfer enhancement factor “beta” ($\beta \geq 1$) is a scalar describing any additional “push” imparted to Dimorphos as a result of escaping ejecta and is planned to be estimated from observations made before, during, and after the event using the approach outlined in Rivkin et al. (2021). The Light Italian CubeSat for Imaging of Asteroid (LICIACube; Dotto et al. 2021), contributed by the Italian Space Agency and deployed from DART in the days before impact, will contribute some of these observations during a fast flyby of the system as the event unfolds.

The European Space Agency mission Hera (Michel et al. 2018, 2022) consists of an orbiter and two CubeSats, called Juventas and Milani, that will visit Dimorphos 4 yr after the DART impact to fully characterize the physical (including interior), compositional, and dynamical states of the system. Hera will also assess the impact effects further, in particular the size and morphology of the crater left by DART and the actual momentum transferred by the impact, in part through actual



Original content from this work may be used under the terms of the [Creative Commons Attribution 4.0 licence](#). Any further distribution of this work must maintain attribution to the author(s) and the title of the work, journal citation and DOI.

measurement of Dimorphos’s mass. Together, DART and Hera are supported by the Asteroid Impact and Deflection Assessment cooperation between the two space agencies.

The size and velocity distributions of ejecta produced by a hypervelocity impact on the low-gravity surface of an asteroid are an important topic for many reasons related to planetary defense and also regolith production on asteroid surfaces. Yet these distributions involve large uncertainties, in particular for the low-speed component that is very difficult to characterize through impact experiments in Earth-surface gravity conditions. Scaling laws have been developed based on dimensional analysis that indicate how multiple parameters of the impact and cratering process relate to each other, allowing predictions and extrapolations for different impact conditions. They allow relating the crater’s radius, as well as the ejecta mass and ejection velocities, to the impact conditions. Depending on whether the surface strength or net surface acceleration accounting for body rotation and body gravity controls the cratering process, the impact is defined as occurring in the strength regime or in the gravity regime, respectively. Laboratory experiments have been conducted in order to obtain the empirical values of the constant parameters employed in the scaling laws for both regimes and for different materials (Housen & Holsapple 2003, 2011). However, scaling laws are idealized, as they assume the uniformity of the process, as well as structural continuity, and they are not valid for the entire ejecta velocity range (Housen & Holsapple 2011). Numerical simulations have also been developed to predict the crater and ejecta properties from an impact, but some situations are very challenging to numerically simulate, such as when the process needs a long time to finalize and involves more than shock physics. Thus, validations of potential modeling improvements for these challenging circumstances are strongly needed.

While impact experiments in the laboratory remain crucial to validate scaling laws and simulations at small scales, experiments at the real scale of an asteroid are required to make sure of their more general validity. The Deep Impact mission was the first mission to perform an actual impact on a comet in 2005, but the outcome was so different than expected that there are still some debates about its interpretation. More recently, the JAXA Hayabusa2 sample return mission to Ryugu (Watanabe et al. 2019) successfully made the first impact experiment on an asteroid with its Small Carry-on Impactor (SCI; Arakawa et al. 2020). The impact of the 2 kg projectile into the surface at 2 km s^{-1} was observed by a small camera called Deployable CAMera 3 that was deployed for this purpose, showing a fraction of ejecta getting back to the surface of the asteroid despite its low gravity. Later, the Hayabusa2 Optical Navigation Camera observed the impact site, allowing the measurement of the crater’s size. While predictions were giving a crater size of a few meters, under the assumption that the impact would take place in the strength regime, the measurements gave a crater diameter of 15 m. Using scaling laws, it was then found that the only way to explain such a large size is if the impact took place in the gravity regime and the surface cohesion was smaller than 1 Pa. This would also explain the observed rather large fraction of low-speed ejecta.

Clearly, whether the impact takes place in the gravity or strength regime can make a big difference, both in the crater’s size and in the ejecta properties. The consequences would also be a difference in the momentum enhancement factor β and the

fate of ejecta. Ryugu is about 900 m in diameter, while Dimorphos is only about 160 m in diameter, and both objects probably have different formation histories. Therefore, it is difficult to assess a priori whether the impact into Dimorphos will be gravity- or strength-dominated, despite Dimorphos’s smaller size. So, we need to allow for both cases. Only later, comparing with the actual DART impact, the ejecta observed by LICIACube, and, eventually, the measurements of the crater’s properties by Hera, we will be able to provide answers to this very important question.

In this paper, we survey work performed within the Ejecta Working Group of the DART Investigation Team to predict the quantity, characteristics, dynamical behavior, fate, and presentation within planned observations (i.e., observability) of the ejecta that will be generated by the DART impact. We start with a discussion of the different phases of ejecta generation and different approaches to use for initializing ejecta in Section 2. Here initialization is taken to mean defining the initial time, vector position, and vector velocity, plus size, density, and mass, of ejecta particles sampled for later dynamical propagation within and away from the binary asteroid system. In Section 3, we discuss the accelerations acting on ejecta within that dynamical propagation and their implementation within different software packages. Additional perturbing effects, which can be particularly important, especially in the initial phases of the ejecta’s motion, are described in Section 4. In Section 5, we detail a methodology by which the size and spatial distributions of ejecta particle number density are turned into simulated images from LICIACube and Earth-vicinity vantage points at planned image-capture epochs. Next, in Section 6, we apply all of these methods to a brief case study of nominal and off-nominal scenarios spanning a range of total ejecta mass and cumulative size–frequency distribution (cSFD) slope. Conclusions are provided and avenues for future work are discussed in Section 7. Finally, the reader is referred to companion papers on the impact physics (Stickle et al. 2022), the binary dynamics pre- and post-impact (Richardson et al. 2022), the ground-based observation campaign (Naidu et al. 2022; Pravec et al. 2022; Scheirich & Pravec 2022), and the use of spacecraft-based observations for geological assessment (Pajola et al. 2022) and shape modeling (Daly et al. 2022) to form a more complete picture of the expectations for the DART encounter.

2. Ejecta Characteristics and Initialization

With an anticipated speed of about 6 km s^{-1} , the DART impact will occur in the hypervelocity cratering regime. This complex process of hypervelocity cratering can be divided into two distinct phases: the impact phase and the phase involving the dynamical evolution of the ejecta, which may include reaccumulation on Didymos and/or Dimorphos (Jutzi et al. 2019). During the first moments of crater formation, highly shocked material is ejected out of the growing crater cavity, carrying away a portion of the energy and momentum budgets.

The difficulty in studying the entire process of crater formation and ejecta reaccumulation is that with the low gravity and strength that are predicted on a rubble-pile Dimorphos, consistent with our current understanding of binary formation and evolution (Walsh & Jacobson 2015), impact-related processes happen on very different spatiotemporal scales. In the case of the DART impact, the cratering process could last from a few seconds to \approx tens of minutes. On

the other hand, the dynamical evolution of the ejecta occurs over even longer timescales, up to several weeks/months (Yu et al. 2017; Yu & Michel 2018).

Very fast ejecta (with speeds up to five times the impact velocity (Kieffer 1977), depending on the angle between the converging surface of the projectile and the target during the “jetting” phase that occurs in the first moments following the impact (Johnson et al. 2014)) will escape from the asteroid system. Very slow ejecta (with speeds much lower than Dimorphos’s escape velocity) will rapidly reaccrete on the source asteroid body. Low- to moderate-speed ejecta that do not escape the system or rapidly reaccrete can survive longer in the binary system, undergoing complex three-body motion, and even stabilize in resonant orbits around Didymos’s libration points (Soldini et al. 2020a). The ultimate fate of such long-term surviving particles depends critically on their size, with smaller dust-sized particles being less stable due to their sensitivity to nongravitational forces, namely, solar radiation pressure (SRP).

2.1. Impact Phase

The complicated process of ejecta formation during cratering involves extreme pressures and temperatures and requires laboratory experiments and dedicated numerical codes to understand.

Numerous past impact experiments (e.g., Gault et al. 1963; Cintala et al. 1999; Anderson et al. 2003; Hermalyn & Schultz 2011; Housen & Holsapple 2011) have shown that the ejecta mass–velocity–launch position distribution is sensitive to target properties—including target strength, density, and porosity—and impactor density and speed. For example, Gault et al. (1963) recorded the mass–velocity distribution of ejecta from impacts into strong basalt (≈ 30 MPa), and Housen (1992) recorded the ejected mass as a function of velocity from impacts into weaker material mixtures (< 1 MPa), including weakly cemented basalt (WCB). The data for solid basalt (a few percent porous) showed steeper mass–velocity trends than in the case of the more porous WCB ($\approx 20\%$ porosity). Similar data exist for impacts into highly porous mixtures of sand and fly ash (Housen & Holsapple 2003) and sand (Cintala et al. 1999; Anderson et al. 2003). Recent impact experiments (Ormö et al. 2022) also noted the influence of heterogeneities within the target. Despite the relatively large number of laboratory-scale impact experiments, it is difficult to quantify the influence of target properties independently. Moreover, it is unknown how well the results of small-scale laboratory experiments can be extrapolated to cratering on asteroids, as these settings are separated by orders of magnitude in both gravity and spatial scale. The specifics of the strength and porosity properties on asteroids are also highly uncertain.

To computationally model a complicated process like impact cratering requires the use of computer codes that can simulate not only the passage of a shock wave but also the behavior of geologic materials over a broad range of stress states. Impact simulations using so-called shock physics codes have been widely used to predict the outcome of the impact of a kinetic impactor (e.g., Jutzi & Michel 2014; Raducan et al. 2019). Such models, if rigorously validated against laboratory experiments, are able to accurately assess the full suite of consequences related to the collision of a spacecraft with an asteroid. Such numerical simulations have the advantage over laboratory experiments that a larger range of events (with a

large range of initial conditions (ICs) and target properties to help account for some of the unknowns), which are more relevant to asteroids, can be tested. Impact simulations of the DART impact have been performed in the context of the DART Impact Working Group (e.g., Stickle et al. 2017; Rainey et al. 2020; Stickle et al. 2022), while systematic studies of the influence of target properties have previously been performed by Prieur et al. (2017), Luther et al. (2018), and Raducan et al. (2019).

2.2. Dynamical Evolution of the Ejecta Phase

N -body codes are needed to model the mid- and long-term evolution of the ejecta. After shock physics–related effects cease, the dynamics of fragments are dominated by the gravitational pull of the asteroids. In such a low-acceleration environment, small dynamical perturbations caused by inhomogeneities of the asteroids’ mass distribution, interparticle interactions, and SRP play major roles in the long-term evolution of ejecta fragments. N -body codes are suitable to reproduce the dynamics of ejecta fragments in this context, as they provide reliable long-term integration of the gravitational and nongravitational acceleration terms involved.

We investigate the dynamical evolution of ejecta using N -body discrete element method (DEM) codes, a subset of N -body codes that account for the finite sizes of N -body particles. It is important to characterize the mutual contact interaction between ejecta fragments, which might collide between each other and form aggregates where several particles remain in stable or quasi-stable contact with each other. Preliminary results using GRAINS, a DEM N -body code that models ejecta fragments as irregularly shaped polyhedra (Ferrari et al. 2017, 2020), have shown that contact interactions between particles are indeed important to their short- to medium-term dynamics (Ferrari et al. 2021). The code `pkdgrav` (Richardson et al. 2000; Stadel 2001) with soft-sphere DEM contacts (Schwartz et al. 2012; Zhang et al. 2017, 2018) has been used to study the gravitational reaccumulation phase after catastrophic and subcatastrophic disruption (e.g., Ballouz et al. 2014; Schwartz et al. 2016, 2018; Zhang et al. 2021a).

As an input, DEM N -body codes require initial-time knowledge of the dynamical state, i.e., the full vector position and velocity, of all fragments and their physical properties, such as mass, volume, or density. In addition, when six degrees of freedom (dof) particles are used, as in the case of GRAINS’s angular fragments, the initial-time orientation and spin state of each particle must also be known.

There are several approaches that can be implemented to define the ejecta properties in an N -body code: (a) empirically derived scaling laws from laboratory experiments, (b) direct handoff from shock physics numerical models, and (c) velocity field transition from shock physics numerical results. These approaches are schematically illustrated in Figure 1. Each of these has their own advantages and disadvantages, as described below.

2.3. Ejecta Initialization

2.3.1. Initialization from Ejecta Scaling Relationships, Previously Calibrated to Laboratory Experiments

One way of initializing the ejecta in N -body codes is to use ejecta scaling relationships, which have been previously calibrated to laboratory experiments. Arguably, the most

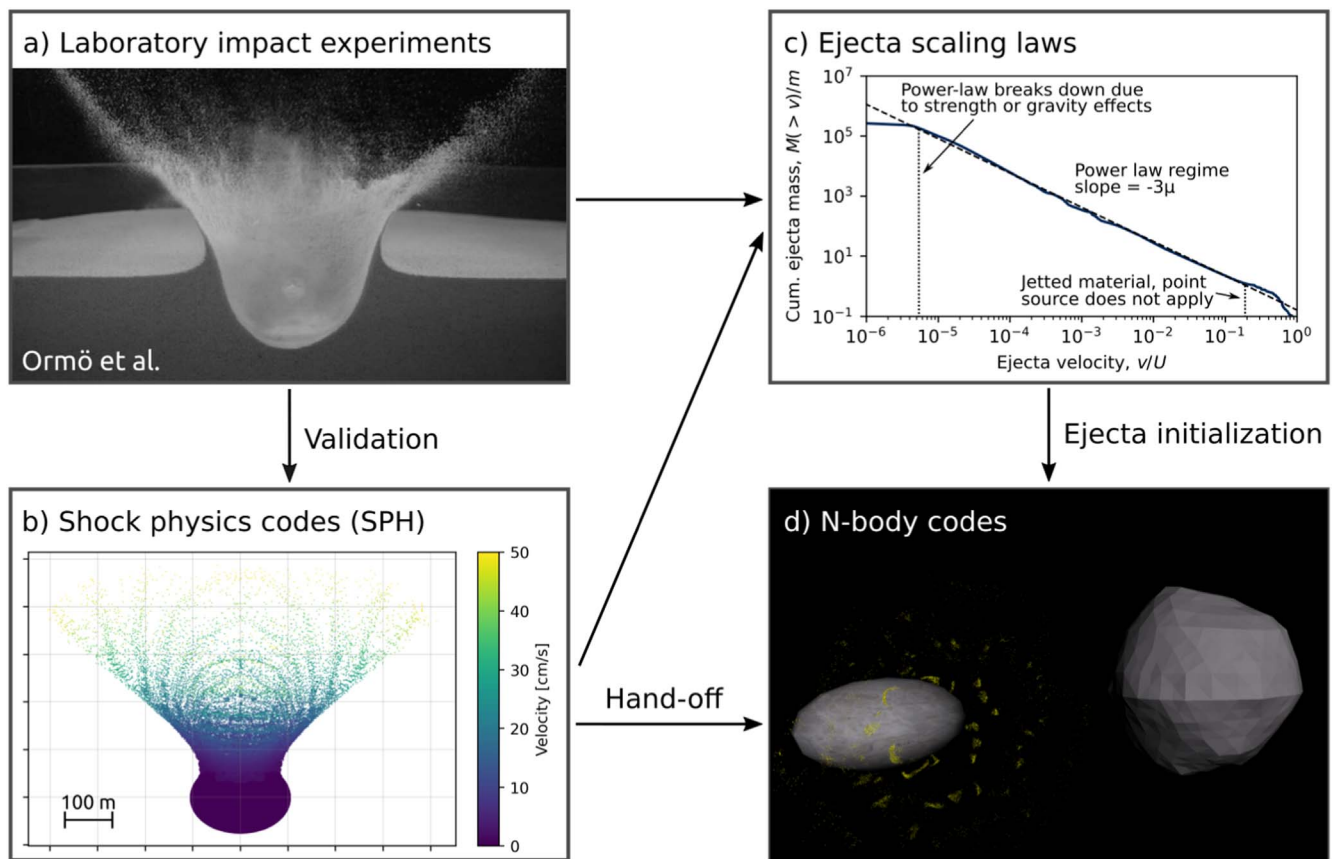


Figure 1. Schematic representation of the handoff procedure and ejecta initialization in N -body codes for mid- and long-term evolution of the DART impact ejecta. (a) Properties of the ejecta plume from small-scale impacts can be recorded from laboratory impact experiments (J. Ormö et al. 2022, personal communication). (b) Shock physics codes (e.g., SPH codes) validated against laboratory impact experiments can be used to model asteroid-scale impacts. (c) Ejecta scaling relationships (i.e., Housen & Holsapple 2011) can be used to approximate the behavior of the ejecta away from the impact point and crater rim using laboratory- or numerical simulation-derived scaling constants (Housen & Holsapple 2011; Raducan et al. 2019). (d) The input conditions in N -body codes that track the mid- and long-term evolution of the DART impact ejecta particles can be initialized by direct handoff from SPH codes or by applying ejecta scaling relationships.

widely used ejecta scaling relationships were derived by Housen & Holsapple (2011) using point-source approximation and dimensional analysis. Housen & Holsapple (2011) proposed a series of power-law scaling equations that relate the initial impact conditions to properties of the impact ejecta, such as mass, speed, and launch position distributions. In reality, the ejecta velocity–launch position distribution deviates from a simple power law close to the impact point and near the crater rim. In the Housen & Holsapple (2011) formulation, the ejecta scaling deviates from a simple power law near the crater rim, where the ejection speed is reduced to zero as the ejection flow is increasingly affected by gravity or strength. Recent modifications (Raducan et al. 2019) also account for the behavior of very fast ejecta launched close to the impact point. The Housen & Holsapple (2011) ejecta scaling relations include a number of constants that are determined by fitting the equation to empirical data (e.g., the velocity exponent μ , density scaling exponent ν , or constant C_1). Housen & Holsapple (2011) gave a comprehensive summary of ejecta data from the literature for a variety of target materials and the corresponding scaling constants.

This method has been used to initialize ejecta properties and integrate the ejecta evolution in an idealized case of an isolated, spherical Dimorphos without SRP by Schwartz et al. (2016). Their preliminary study came out of an effort to develop the methodology to diagnose and characterize safe regions to

position a proposed observer spacecraft during the time of the DART impact (Michel et al. 2016, 2018). Schwartz et al. (2016) also contained an early hydrocode-to-soft-sphere DEM N -body handoff methodology (discussed below), which has since been built upon in Ballouz et al. (2019) and Zhang et al. (2021a).

One obvious advantage of using ejecta scaling relationships to initialize the ejecta in N -body codes is their simplicity; they do not require the use of additional computer codes, which introduce many additional parameters and the complication of developing a technique to translate the code output into ICs for N -body integration. However, data from only a limited number of laboratory experiments are available, and these were performed under a limited range of impact conditions (i.e., all under Earth-surface gravity and at small scales), which might not always be justifiably extrapolated to asteroid environments. Moreover, the scaling relationships are an idealization of the ejecta behavior and do not account for the variation of the ejection angle with material properties (initialization conditions usually assume an ejection angle of $\approx 45^\circ$). Recent studies (i.e., Raducan et al. 2022) have shown that the ejection angle from a high-velocity impact on an asteroid deviates from 45° depending on the target friction properties and impact angle. In addition, the ejecta scaling laws do not account for preexisting heterogeneities within the target

or target curvature (which is important for very large craters relative to the target).

2.3.2. Direct Handoff from Discrete Particle Shock Physics Codes

Another approach is to use shock physics numerical simulations to model the impact crater, and then assign the ejecta properties as ICs to N -body codes. This method has been used to link Bern’s smoothed particle hydrodynamics (SPH) simulations to GRAINS. Once the impact phase is over, the shock physics code simulations are stopped, and the SPH particles and their corresponding velocity and mass distribution are fed into the N -body code that computes the dynamical evolution of the system to later times. In the case of a DART-like impact, the shock physics code is stopped when no more ejecta is produced with velocities higher than a few centimeters per second (approximately the escape velocity of Dimorphos at its surface, $v_{\text{Dim}} \approx 0.089 \text{ m s}^{-1}$), after which the ejected particles are affected only by gravity. The handoff time is representative for the transient morphology of the target. For a DART-like impact, the transfer time varies with crater growth time and cratering efficiency and ranges from \approx a few seconds after the impact (for strong, $>1 \text{ kPa}$ targets) to \approx tens of minutes after the impact (for low-cohesion targets). The SPH particles are directly transformed into DEM particles, and their mass and density are kept constant. Note that cohesion is not handed over to the N -body simulation; therefore, the particles are cohesionless.

One of the main current limitations of this approach is that the ejecta particle size distribution is not considered. Due to the limits in the resolution in SPH simulations, the ejected fragments are not explicitly resolved. Instead, the SPH particles do not represent “real” mass particles, and the material needs to be further discretized, conserving the combined ejecta mass, into smaller particles within the N -body code. Another difficulty, discussed within Schwartz et al. (2016), is the need to avoid having any overlap of the resulting particles within the N -body code, which would produce unphysical particle repulsion forces depending on the particle interaction model (e.g., “hard-sphere” versus “soft-sphere”). This may involve shrinking particle volumes and increasing particle densities while conserving particle masses.

2.3.3. Handoff Based on Velocity Field Transition from Shock Physics Numerical Results

The initial mass–velocity distribution of the ejecta is a key that determines their later evolution. As discussed in Section 2.3.1, the ejecta velocity scaling laws are nevertheless limited by the point-source approximation and the lack of validation with regolith target materials under low gravity. Numerical modeling using well-validated shock physics codes may provide a more reliable way to characterize the ejecta mass–velocity distribution.

Therefore, in addition to the direct particle-to-particle handoff procedure described in Section 2.3.2, we can also use a velocity field transition procedure to carry out the handoff (Zhang et al. 2021a). This procedure consists of four steps. First, a regolith bed is generated with a desirable particle size distribution and settled down under a predefined gravity environment using a DEM code. Second, according to the ejecta velocity field given by a shock physics simulation, a surface is constructed to isolate the compact material from the

fast-moving ejecta using the α -shape-construction algorithm (Ballouz et al. 2019). Third, this surface then is used to carve out the DEM regolith bed and match the velocity and mass of particles with the shock physics simulation outcome. Finally, the fast-moving ejecta is added as individual particles.

With a combination of two numerical schemes, Bern’s SPH and the DEM code `pkdgrav`, this handoff procedure was developed recently for end-to-end impact cratering modeling and has been validated against the Hayabusa2 SCI impact experiments on asteroid Ryugu (Zhang et al. 2021a). The simulation results show that, in this low-gravity regime, the excavation process lasted about 300 s. After that, the ejecta curtain started to deposit onto the surface. It took above 1000 s to let most of the ejecta settle down. The time evolution of the ejecta is quantitatively consistent with the results of the SCI impact (Arakawa et al. 2020). The final crater morphology also shows quantitatively good agreement, where the crater depths are identical and differences in the crater diameters are less than 1 m. These simulation results confirm that the SCI impact occurred in the gravity-dominated regime, and the cohesion of Ryugu’s surface regolith is extremely small (Zhang et al. 2021b).

In this handoff procedure, the particle resolution and size distribution in the DEM simulation are independent of those of the SPH simulation. Therefore, the ejecta distribution can be refined or resampled according to the mass–velocity relationship and launch position to reflect the actual size distribution of the ejecta fragments. The adopted particle resolution would be a trade-off between the computational cost and simulation fidelity requirements. In addition, as the late stage of crater growth is modeled using a presettled regolith bed, the overlapping issue in the direct handoff method can be eliminated, and the seismic dynamics of granular material following the high-speed impact can be revealed, which is one of the big advantages of this handoff procedure.

However, since this handoff procedure considers both the ejecta field and the compacted materials that have not been ejected, the appropriate time to carry out this handoff is largely uncertain. As shown in the SCI impact simulations (Zhang et al. 2021b), due to the propagation of impact momentum, particles with low-to-moderate velocity located $>5 \text{ m}$ from the impact site were still continuously ejected from the surface 200 s after the impact. The long-lasting growth of the ejecta curtain may affect the dynamics of Dimorphos and the deflection efficiency measurement (i.e., β), which needs to be carefully tested using the handoff numerical framework.

3. Ejecta Dynamical Propagation

The subsequent motion of the ejecta particles is driven by gravitational and nongravitational forces that are acting with different relative importance depending on the distance from the asteroids and the size and mass of the particles themselves. To begin with, the main acceleration is due to the gravity of the two asteroids in the binary system. Either the primary (i.e., Didymos) or the secondary (i.e., Dimorphos) can be placed at the center of the reference frame, while the effect of the other is treated as a third-body perturbation. The gravity of both Didymos and Dimorphos can be modeled, as a first approximation, as a point mass (Vallado 2013). Nonetheless, both bodies have a nonspherical shape; hence, higher-order effects influence the motion of the particles when they are close enough to either body. Therefore, the gravitational potential has

to be expressed with a more sophisticated approach. The bodies can be approximated by triaxial ellipsoids, and the potential can be computed with analytical expressions (e.g., Murray & Dermott 2000) or by means of spherical harmonics (e.g., Vallado 2013). More complex body shapes can be approximated by means of polyhedra with a suitable number of faces (Werner & Scheeres 1997) or by a mascon model (e.g., Rossi et al. 1999; Soldini et al. 2020a). Due to computer time requirements, the more complex models, such as the polyhedron, should be used only when the particles are close enough to the central body to be perturbed by its nonspherical features, switching to the analytical expressions when the distance from the central asteroid exceeds a few body radii (Rossi et al. 1999). Note that the case of mascons can also be relevant for evaluating how the internal structure of Didymos and Dimorphos affects the evolution of the ejecta particles.

Apart from the two binary components, the other most relevant gravitational perturbation is due to the Sun. The position of the Sun can be taken from precise ephemerides (such as, e.g., kernels for use with the SPICE Toolkit; Acton et al. 2018) or analytically computed from a reference orbit.

The effect of the SRP acceleration has to be considered carefully. As is well known, its magnitude is proportional to the ratio between the area and the mass of the particles (see, e.g., Milani et al. 1987). For small particles, below about 1 mm, the SRP can become the dominant acceleration, prevailing over the gravity attraction from the two asteroids, and is able to quickly sweep out those objects from the system (Rossi & Fulchignoni 2007). As a first approximation, the particles can be considered as spheres, in the so-called cannonball model (e.g., Vallado 2013). In a more accurate modeling effort, the ellipsoidal shape of the particles and their rotation is considered. The rotation of the ellipsoidal shape changes the aspect ratio of the particle with respect to the Sun and hence the area over mass ratio of the object, causing a modulation of the SRP with time. The shadow, caused by either asteroid passing between the Sun and the particle and switching off the SRP perturbation for a while, is modeled as well.

Different software packages used for the DART ejecta studies implement the above-described models. These packages include the following.

1. The gravitational orbits Near Earth Asteroid Regions (`gONEAR`) is an N -body planetary propagator originally developed for the Hayabusa2 trajectory design, used for the prediction of Hayabusa2's ejecta after the SCI impact (Saiki et al. 2017; Soldini et al. 2020a) and validated with real-time data during Hayabusa2's superior solar conjunction phase (Soldini et al. 2020b, 2020c).
2. The LICIACube Ejecta Integrator (`LICEI`), developed in the framework of the LICIACube science team and described in Rossi et al. (2022), is a simulation code integrating the orbits of the ejecta, modeled as rotating ellipsoidal particles, taking into account all of the abovementioned perturbations. In particular, the gravity field from the central body (either Didymos or Dimorphos) can be computed by means of the polyhedral approach (Werner & Scheeres 1997) or a simpler approximation of an analytic triaxial ellipsoid gravity field based on McCullagh's formula (Murray & Dermott 2000). The switch distance between the two gravity representations is an input parameter to the code, and the simulations show a smooth transition between the two

representations (see Rossi et al. 2022 for details). The gravity from the secondary body is always computed by means of the analytic ellipsoidal approach (note that the `LICEI` simulations presented in Section 4 are computed with the analytical approach because they are devoted to exploration of the SRP effects). The mutual interaction of the ejecta particles is not accounted for. The solar tides are computed considering an analytic solar orbit. As detailed in Section 4, the SRP effect is computed considering rotating ellipsoidal particles and the shadow (without penumbra) from the ellipsoidal approximated shapes of the two asteroids. No additional nongravitational effects (e.g., Poynting–Robertson) are accounted for due to their limited influence on the considered problem (see, e.g., Yu et al. 2017). Finally, the numerical integration is performed by means of the Radau integrator with variable step size, particularly well suited for the handling of close approaches (Everhart 1985).

3. The restricted full three-body problem (RF3BP) propagator developed at the Jet Propulsion Laboratory (JPL) starting circa 2009 served as a template for the methodology presented in Yu et al. (2017). This parallelized C++ code integrates ejecta as noninfluencing test particles (hence the “restricted” in its name) without any interparticle interaction, be that gravitational, collisional, or otherwise. However, it integrates these ejecta particles within a high-fidelity model of the binary asteroid system itself (hence the “full” in its name). The full two-body problem state of the binary previously propagated using GUBAS (a simple, fast, and open-source tool available as a free download¹⁶; Davis & Scheeres 2020) is read in and time-interpolated. Ejecta particles experience polyhedral gravity (Werner & Scheeres 1997) from both binary components up to a user-input distance (150 km, or about two Hill radii) from the system barycenter and then point-mass gravity from both binary components beyond that distance. The Didymos system barycenter also serves as the origin of the integration reference frame. A simple conic reference orbit of the Didymos barycenter from Horizons¹⁷ places the Sun for calculating point-mass gravity solar tide perturbation and SRP. Ejecta are modeled as simple spherical particles with cannonball SRP but shadowing calculated from the full polyhedral shape models. Any collision with either extended body is detected and pinpointed upon the same shape models. The code utilizes a standard (i.e., nonsymplectic) variable step size RKF7(8) integrator (Fehlberg 1968) and outputs ejecta states in an efficient binary format at user-requested intervals.

In Yu et al. (2017) and Yu & Michel (2018), the effects of the relevant forces on the evolution of an ejecta cloud from a binary asteroid were explored and evaluated. In particular, in Yu & Michel (2018), a classification of the orbits as a function of the ejecta fates, e.g., a collision with one of the binary components or the escape from the region of influence of the system, was performed. A grid search of various launching sites of ejecta over the globe of Dimorphos, considering a wide range of possible ejection speeds, was performed too,

¹⁶ <https://github.com/alex-b-davis/gubas>

¹⁷ <https://ssd.jpl.nasa.gov/horizons/>

determining the dependency of the ejecta fate on launching sites (projectile impact sites) and speeds. Additional perturbing effects, which can be particularly important, especially in the initial phases of the ejecta motion, are described in the next section.

4. Additional Dynamical Effects Explored

In this section, we review some dynamical effects coming from different physical properties of the particles that can influence the propagation of the ejecta. In particular, we investigate what the nonsphericity, rotation, and temperature of the particles can introduce to the motion of the ejecta. We will address to what extent the spherical particle approximation remains valid and sufficient in case of rotation. We expect that low particle elongation, close proximity to the surface of the body, and fast rotation will eliminate any bias on the ejecta plume dynamics due to the spherical particle approximation. To describe the effect of the aforementioned physical properties of the particles, we performed numerical simulations with three different codes, considering ellipsoidal shape particles applied to the nominal case of Section 6. The results are reported in terms of particle rotational frequencies, velocity dispersion, and spatial dispersion under the same input impact conditions. In addition, velocity dispersion owing to different particle temperatures and collisions between particles is discussed.

The three codes that have been used to study the additional dynamical effects are as follows.

1. **GRAINS** (Ferrari et al. 2017, 2020): a DEM N -body code that models the ejecta fragments as tiny polyhedra with a randomized shape. Therefore, it has an advantage over other N -body codes such as `pkdgrav` or `Rebound` in that it allows for more complex particle shapes that may significantly affect the nature of particle collisions. The full six-dof dynamics, including both center-of-mass (translational) and attitude (rotational) motion of ejecta, are considered. Each particle undergoes the effect of an environmental gravity field (point-mass Didymos and Dimorphos), and the particles also interact with each other via point-mass mutual gravity, contact, and collisions.
2. **LICEI**: a simulation code briefly described in Section 3 (see also Rossi et al. 2022 for details).
3. **LICIACube Model for Aspherical Rotating Dust Ejecta** (LIMARDE; Ivanovski et al. 2022): a 3D+t nonspherical dust model that solves the Euler dynamical and kinetic equations. Different shapes, initial particle orientations, and velocities, as well as torque, are considered. The particles are assumed to be homogeneous, isothermal convex bodies having the same physical properties of Dimorphos's surface where applicable. The dust motion starting from the initial dynamical parameters (speed, orientation, and torque) is governed by SRP and point-mass Didymos and Dimorphos gravity, with collisions approximated by the interaction between the ejected particles and infinitesimal gas drag (even though no gas is expected to be present).

4.1. Transient Collisional Phase

Shortly after impact, the ejecta particles will be very close to each other and likely undergo a transient collisional phase. We performed numerical simulations using **GRAINS** to assess the

likelihood of mutual ejecta collisions and quantify their frequency. Also, we provide an estimate of the duration of this early collisional phase. We use initial ejecta conditions provided by scaling laws, as described in Section 2.3.1 (also referenced as IC particles in the following). These provide information on the position, velocity, mass, and diameter of spherical ejecta particles at their time of ejection after the DART impact. This information is used to initialize the **GRAINS** N -body code. While the position and velocity of each IC particle can be forwarded directly to the N -body code, the initialization of their polyhedral shape and density requires an intermediate step to hand off information from IC particles to N -body fragments. The N fragments are generated, each with a random polyhedral shape, with aspect ratios in the $[0.7-1]$ range and approximately 10 vertices. The mean size of each N -body fragment is adjusted to match the size of its corresponding IC particle. Subsequently, the density of each N -body fragment is adjusted to match the mass of its corresponding IC particle.

The occurrence of collisional events between particles in the ejecta cone is driven by the number of fragments per unit area and their interparticle distance. This can be measured quantitatively in terms of surface density; assuming a bidimensional particle flow on the cone surface, we define surface density as the mass per unit area on the cone. Also, the investigation can be limited to a subset of the ICs to improve computational efficiency and without any loss of generality. Therefore, with reference to ICs provided for the nominal case in Section 6, we consider a small section of the full disk, 10° wide and $0.15R$ deep, where R is the radius of the disk (red area in Figure 2(a)). This patch contains approximately 10,000 particles with an average surface density of 133.5 kg m^{-2} . We simulate the dynamics of the particles within the patch as they interact through mutual contacts and collisions. Additionally, we investigated the effect of a lower surface density by reducing the number of particles in the patch using a dedicated algorithm that preserves the overall statistical properties of the particles (i.e., subsamples are extracted from the 10,000 particles in the patch, always keeping the same size distribution over 20 size bins). Figure 2(b) shows the number of collisions in time for several values of surface density. In this case, the transient collisional phase lasts for a few minutes only, with the major contribution occurring within the first tens of seconds. As expected, a lower surface density implies a lower number of collisions between fragments and an earlier termination of the transient phase.

4.2. SRP Effect in Close-field Environment

As mentioned in Section 3, SRP is one of the main perturbations determining the evolution of the small particles. In **LICEI**, it is possible to consider the effect of SRP over either spherical or ellipsoidal rotating particles. Ellipsoidal rotating particles expose a different area to the SRP, thus experiencing a different acceleration, changing with time. The rotation can be either a regular one around the principal axis with an assigned period or a random tumbling motion. Therefore, first, the 10,000 spherical particles in the circular section are propagated for 300 s considering the particle radius as listed in the IC file. Then, for each particle, an equivalent triaxial ellipsoid (having the same volume as the original spherical particle and axis ratios $b/a = 0.9$ and $c/a = 0.8$) is derived from the value of the radius listed in the IC file. These

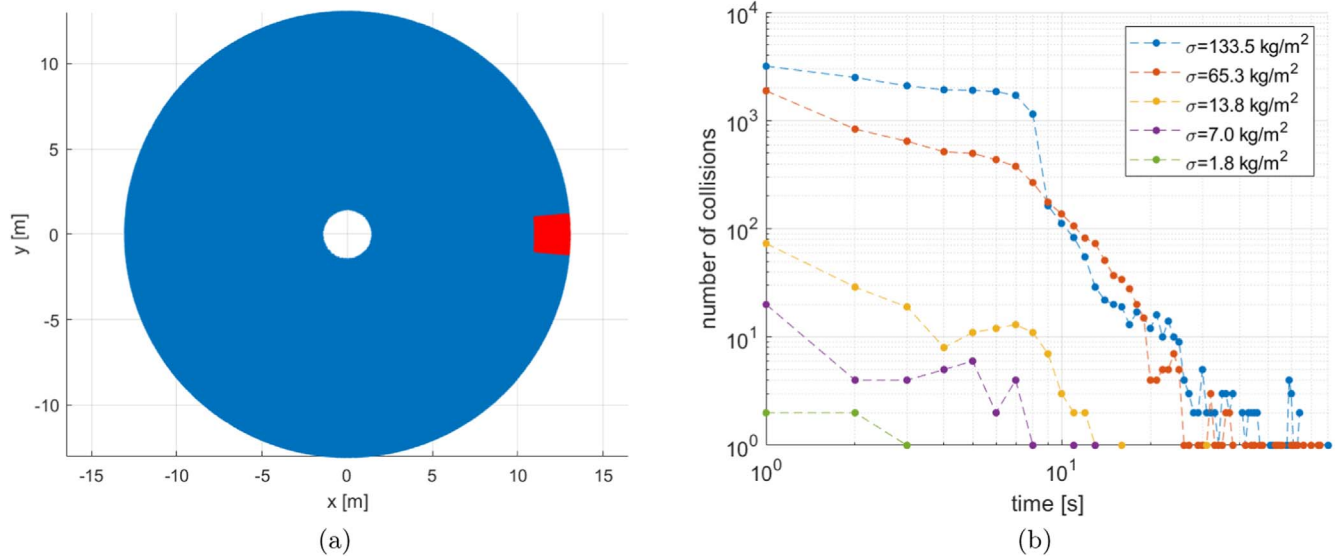


Figure 2. (a) The ICs from scaling laws (Section 2.3.1) are shown in blue; the patch used to characterize collisions is shown in red. (b) Number of collisions in time during the early transient collisional phase for different values of surface density σ .

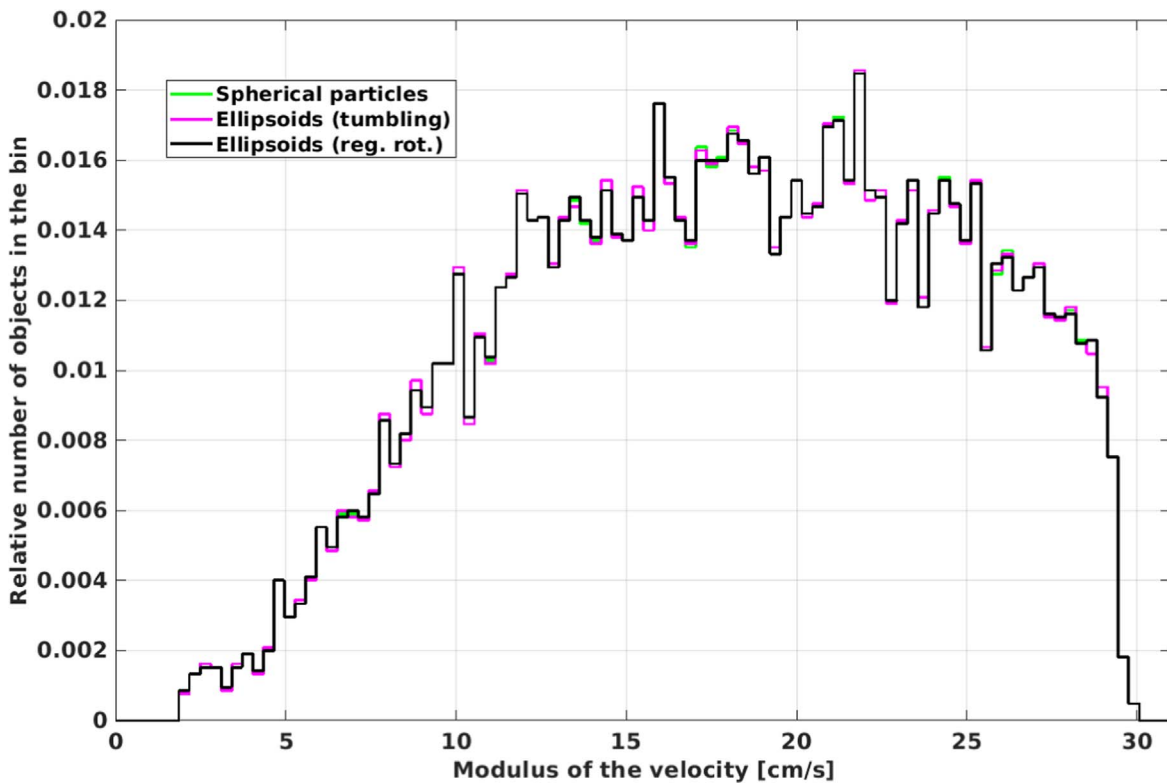


Figure 3. Distribution of the ejecta velocities after 300 s as propagated with three different SRP models (see text for details). The Y-axis shows the number of objects in each bin relative to the total of 10,000 test particles. Note that, as explained in the text, the distributions match up for most of the plot; hence, only the black line is usually visible.

10,000 ellipsoidal particles are then propagated assuming both regular rotation and random tumbling. Figure 3 shows the distribution of the velocities of the particles after 300 s. The green line refers to the spherical particles, the black line to the ellipsoidal particles with regular rotation, and the magenta line to the tumbling ellipsoids. As expected, in such a short time span, when the particles are still close to the surface of the body, the three models for the SRP do not display significant

systematic differences. We also note that in the present simulations, we assumed fairly regular particles. For more elongated irregular particles, the difference between the effects can, of course, be enhanced. Nonetheless, the largest difference between the three SRP models can only be appreciated further away from the central body, where the ratio between the amplitude of the SRP and the gravitational accelerations becomes larger.

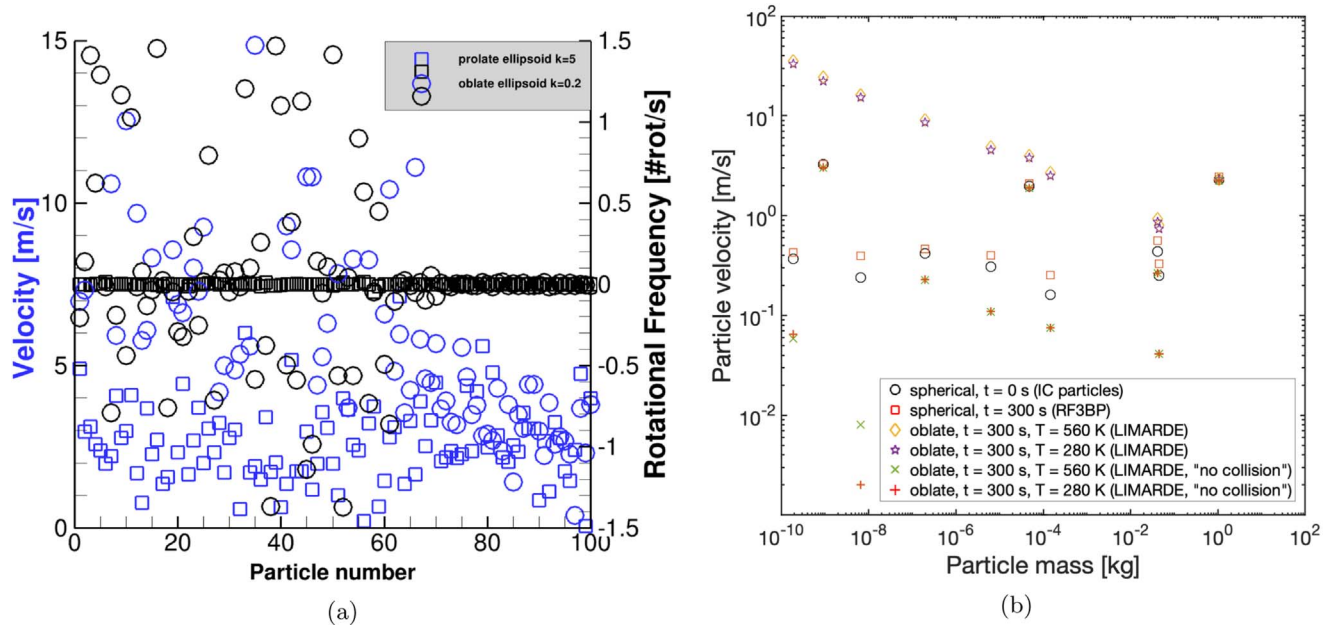


Figure 4. (a) Velocity distribution and rotational frequencies of the oblate ($k = 0.2$) and prolate ($k = 5.0$) equivalent-mass particles derived from 100 spherical IC particles. (b) Temperature and collisional dependence of the velocity achieved by oblate ($k = 0.2$) equivalent-mass particles derived from 10 spherical IC particles as a function of their mass.

4.3. Particle Rotation for Different Dust Temperature in the Collisional Regime

The LIMARDE code can study the motion of irregular dust particles considering their rotation, temperature, initial velocity and torque, and orientation. Here we focus on some additional dynamical effects that might come from the different physical properties of the particles, such as temperature, shape, and density. The code is able to compute the rotational motion of the ejected particles as a function of the active forces at any instance/distance during the propagation of the plume. Torque is computed from the law of variation of the angular momentum by using the Euler dynamic equations. In contrast to the LICEI code, LIMARDE computes the rotation frequency at every time step, avoiding a constant rotation rate subject to change only due to SRP. The triggering of the rotation can be caused by the initial torque, initial velocity, collisions, and the interplay between the work done by the gravity force of Didymos and Dimorphos and SRP. LIMARDE can mimic a collisional regime assuming mutual collisions with smaller particles that can cause drag to the dust particles that constitute the ejecta plume. The rotation is computed along any of the three principal axes of inertia. For the purposes of this paper, we further scaled the particle distribution down to 100 particles, keeping the distribution over the 20 size bins. We considered prolate ($k = 5$) and oblate ($k = 1/5$) asymmetrical ellipsoids of the same mass and density as their spherical equivalents. Both families of particles are propagated for 300 s, having the particle radius, initial velocity, and position of the IC particles (SRP is not considered). Figure 4(a) shows the distribution of the velocity and the rotational frequency of these 100 particles after 300 s. There is clear evidence that the oblate particles achieve a higher speed than their elongated analogs. Importantly, the rotational frequency of the particles of both families is completely different; the majority of the oblate particles rotate, while the elongated ones do not. Therefore, the particle

shape plays a role in the dynamics and spatial distribution of the ejected particles.

Another dynamical effect that we investigated with LIMARDE is the effect of the temperature of the particles. We took a sample of 10 IC particles with widely varying mass and performed the following test: similar oblate ($k = 1/5$) particles of equivalent mass to the spherical particles were propagated for 300 s but with different temperatures (280 and 560 K) both with and without the drag approximating collisions. Figure 4(b) shows the comparison of the velocities achieved. The simulation results suggest that there is a cutoff where the temperature stops playing any role, namely, the smaller the particle mass, the higher the velocity dispersion owing to the particle temperature. In particular, for this sample of IC particles, this cutoff is about 0.1 kg.

We would like to outline some of the uncertainties that the described additional dynamics could introduce in particle trajectories. We have reviewed the effect of collisions, nonsphericity, and the temperature of the particles. Collisions can increase the rotational and kinetic energy of the particles and change the velocity distribution up to a few tens of percent. The nonsphericity plays a role shortly after the impact owing to the collisions, even in the absence of initial rotation and velocity, and farther away from the central body, where the ratio between the amplitude of the SRP and the gravitational accelerations is significant. The temperature of the particles might introduce a small dispersion on the velocity for particle masses smaller than 0.1 kg due to the coupled effect of the particle shape and high temperatures (e.g., 560 K).

4.4. Possibility of Low-speed Ejecta Lofting from Distal Locations on Dimorphos

There are two critical speeds to discuss the outcome of the low-speed ejecta: (i) the escape velocity on the surface of Dimorphos, $v_{\text{Dim}} \approx 0.089 \text{ m s}^{-1}$, and (ii) the escape velocity from the binary system (at the distance of Dimorphos from

Didymos), $v_{\text{Sys}} \approx 0.24 \text{ m s}^{-1}$. On one hand, if the particles are launched with an outgoing speed v (positive radial component with respect to the center of mass of Dimorphos) lower than v_{Dim} , they will fall back onto Dimorphos. If launched with an outgoing speed between v_{Dim} and v_{Sys} , the particles will be moving in the binary system and may eventually collide with one of the two bodies. Instead, if there is enough time for SRP to act, small particles could be removed from the system. On the other hand, if a particle's speed is larger than v_{Sys} , it will escape from the binary system with a velocity at infinity (v_{∞}) given by $v_{\infty}^2 = v^2 - v_{\text{Sys}}^2$.

In G. Tancredi et al. (2022, in preparation), we analyze an additional effect: the lofting of material at low speed as a consequence of the generation of seismic waves that propagate into the interior of Dimorphos and, even if highly damped, generate shaking at distant surface points. To analyze this effect, we divide the process into the following steps: (i) generation of impact-induced seismic waves and propagation into the interior of the body, (ii) arrival of these waves coming from the interior to the surface at points located far from the impact point, (iii) shaking produced by the arrival of these waves on small particles located on the surface, (iv) lifting of particles due to shaking and ejection at low speed (comparable to the escape velocity), (v) evolution of particles under the influence of gravity and SRP, and (vi) prediction of the observation of this cloud of particles from the Earth (Moreno et al. 2022).

We anticipate the following potentially observable effects: (i) generation of a cloud of small particles that will produce a hazy or fuzzy appearance of Dimorphos's limb detectable by LICIAcube, (ii) a brightness increase of the binary system due to enhancement on the cross section produced by the cloud of particles, and (iii) generation of a dust trail, similar to those observed in activated asteroids, that can last for several weeks after impact. A numerical prediction of the detectability of these effects will be strongly dependent on the amount and size distribution of the ejected particles, which are largely unknown. On the other hand, in case these effects are observable, an inversion method can be applied to compute the amount of ejected material and discuss the relevance of the shaking process, as well as some elastic and structural parameters of Dimorphos.

5. Ejecta Presentation in Simulated Images

In this section, we detail a methodology by which the time-evolving size and spatial distributions of ejecta particle number density are turned into simulated images from LICIAcube and Earth-vicinity vantage points at planned image-capture epochs. This particular methodology was developed by the lead author and collaborators at JPL. Ejecta are initialized according to crater scaling relations as discussed in Section 2.3.1, with the additional specification of ejection angle as a function of crater footprint radius per polynomial fit given in Cintala et al. (1999). The ejecta are then propagated using the RF3BP propagator briefly described in Section 3 to produce the states of particles in single-precision binary format at user-specified intervals in time in a set of ejecta simulation output files. The resulting particle trajectories merely statistically sample the far larger full population of particles expected from the DART impact. For generation of synthetic images, we need to model the light scattered by the full population. One may scale the actually propagated population to the full population by

considering each propagated particle to represent a ‘‘packet’’ of similarly sized particles, the number of which is given by some size-dependent particle multiplier, K , derived as follows.

We assume a particle cSFD as a function of particle diameter d in power-law form. The number of particles having a size greater than d is given by

$$N(>d) = N_0 d^{-a}, \quad d_{\text{min}} \leq d \leq d_{\text{max}}. \quad (1)$$

Here the cumulative number slope $-a$ is a key quantity controlling the relative abundance of small and large particles. Reasonable values for a range between 2 (shallow) and 3 (steep). The best fit for solid fragments in the returned Itokawa sample was $a = 2.31$ according to Nakamura et al. (2012). As discussed in Cheng et al. (2020), $a \approx 3$ is consistent with boulder size distributions on Itokawa at meter scales and larger (Tancredi et al. 2015; Mazrouei et al. 2014), the data in Nakamura et al. (2012) for solid fragments larger than a micron, and impact experiments (Buhl et al. 2014).

Similarly, we assume a probability distribution function for mass as a function of d to have the power-law form

$$\text{pdf}(m(d)) = C_m d^{-a'}. \quad (2)$$

We can then derive that the fraction of the total ejecta mass, f_{d_1, d_2} , between two diameters d_1 and d_2 , $d_1 < d_2$, is given by

$$f_{d_1, d_2} = C_m \frac{d_2^{-a'+1} - d_1^{-a'+1}}{(-a' + 1)}. \quad (3)$$

Applying this over the full range of particle diameters lets us solve for the constant C_m as

$$C_m = \frac{-a' + 1}{d_{\text{max}}^{-a'+1} - d_{\text{min}}^{-a'+1}}. \quad (4)$$

Now let the full range of particle diameters be divided into n_{bin} logarithmic size bins such that the i th size bin spans the interval $[d_i, d_{u_i}]$. The particle multiplier K_i to apply to each propagated particle falling in the i th size bin is the ratio of the total number of particles we should have in the interval $[d_i, d_{u_i}]$ to the N_i propagated particles in that interval. Therefore,

$$K_i = \frac{1}{N_i} (\text{full \# of particles in interval } [d_i, d_{u_i}]) \quad (5)$$

$$= \frac{1}{N_i} \left(\frac{\text{total mass of ejecta}}{\text{avg. mass of particle in interval } [d_i, d_{u_i}]} \right) \times (\text{fraction of total mass in interval } [d_i, d_{u_i}]). \quad (6)$$

The total mass of the ejecta is given by crater scaling relationships as $k \rho_B R^3$ (Housen & Holsapple 2011), where k is a dimensionless scaling parameter, ρ_B is the target bulk density (or, more correctly, the target surface material density), and R is the final crater radius. The average volume V_{ave} of a particle in the interval $[d_i, d_{u_i}]$ is

$$V_{\text{ave}} = \frac{\pi}{3 \left(\frac{1}{d_{u_i}^3} + \frac{1}{d_i^3} \right)}. \quad (7)$$

Multiplying this average volume with the particle grain density ρ_{grain} and substituting into Equation (6), also applying

Table 1
Specifications for Cameras Used in the Generation of Simulated Images

Platform/Camera	Pixel Dimensions	iFOV	FOV	Focal Length	F/N	λ Passband
LICIACube/LEIA (PL1, NAC)	2048 × 2048	25 μ rad	(2°934) ²	222.5	3	450–900 nm
LICIACube/LUKE (PL2, WAC)	2048 × 1088	78 μ rad	9°153 × 4°862	70.5	2.2	450–700 nm
HST/WFC3-UVIS	1024 × 1024	0.194 μ rad	(0°0114) ²	57,600	24	350–800 nm

Note. LEIA is a panchromatic imager, while LUKE has a Bayer-type red–green–blue filter, and WFC3-UVIS uses the F350LP filter.

Equation (3), we have that

$$K_i = \frac{3 k \rho_B R^3}{N_i \pi \rho_{\text{grain}}} \left(\frac{1}{d_{u_i}^3} + \frac{1}{d_{l_i}^3} \right) \times C_m \left[\frac{d_{u_i}^{-a'+1} - d_{l_i}^{-a'+1}}{(-a' + 1)} \right], \text{ for } i \in \{1, 2, \dots, n_{\text{bin}}\}. \quad (8)$$

Note that it can be verified that the value of the differential mass slope a' here will produce a value of the cumulative number slope a in Equation (1) according to $a = a' + 2$.

Applying these particle multipliers to the propagated particle trajectories, we can construct the time-evolving four-dimensional (4D; by which we mean three spatial dimensions plus the added “dimension” of particle diameter) distribution of the ejecta particle number density for the full population, as well as just the propagated population. Seeking an efficient way to represent this, we developed a size- and spatially discretized interface file (hereafter “cube file”) generated using a recursive subdivision algorithm. The details of this approach are given in [Appendix](#), and it is used all over again to make a time-independent cube file for each planned image-capture epoch postimpact. In summary, we (a) define a base grid with cubical cells that encompasses the entirety of the ejecta at that epoch in its first octant, duplicated for each considered size bin; (b) loop through each unique nonempty 4D base cube calculating the propagated and full-scale population quantity of interest (of which number density is just one option); and (c) attempt subdivision until we no longer maintain a minimum number of propagated particles within nonempty subcubes, meet a uniformity condition for the full-scale population quantity of interest across nonempty subcubes, or hit a maximum level of subdivision.

We then use a script to process a specified cube file’s contents into image data arrays for a specified camera with its associated camera specifications. Table 1 gives the relevant camera specifications used for the case study of the next section. This script loops over the nonempty cubes (be they base cubes or subcubes) in the cube file and maps onto pixels of the image plane (a) the volume of space within the current cube intersected by each pixel column, (b) the number of particles in that volume of space, and (c) the flux from those particles computed using a simple photometric light scattering model. This script can accommodate binning of the pixels in the image plane for efficiency, i.e., forming larger pixels out of $n \times n$ raw pixels. SPICE Toolkit (Acton et al. 2018) calls are used to calculate the observation geometry, including the positions of the camera, the Sun, Earth, Dimorphos, Didymos, and the Didymos system barycenter (with respect to which the origin of the cube file’s base grid is specified in the cube file header). This uses SPICE kernels provided through the DART Science Operations Center (SOC) web page matching the

Design Reference Asteroid (DRA) v3.21 and Design Reference Mission (DRM) v4.01 that were current at the time this work was performed (the digital archive of kernels used is available at Fahnestock & Chesley 2022). When the camera selected is on board the Hubble Space Telescope (HST), the position of Earth’s center is used to approximate HST’s actual position without much loss of fidelity given Didymos’s geocentric distance around the impact epoch. Even under the hypothetical situation where HST is moved to the opposite side of Earth within an orbital plane perpendicular to the vector from geocenter to Didymos, i.e., shifted in position by twice the mean orbital radius of HST’s orbit, the resulting angular error in the direction from HST to Didymos is conservatively bounded below 4/2. The SPICE calls are made for the image-capture time specified by the DRM impact epoch plus the time elapsed since impact as recorded in the cube file header. Camera pointing is specified such that the camera boresight aligns with the vector from the camera (observer) to Dimorphos (specifically, Dimorphos’s center). A user-specified twist angle about the boresight is also accommodated. Finally, in addition to outputting the image data arrays, this script outputs the calculated distance from the observer to Dimorphos, the minimum distance from the observer to any cube (represented as an equivalent-volume sphere) taken over all nonempty cubes, and the pixel coordinates of the centers of Didymos and Dimorphos in the image plane.

To model the photometric light scattering by ejecta particles, we use a simple empirical phase function from recent work done with particles shed by Bennu, as detailed in Hergenrother et al. (2020). See in particular Table 1 and Figure 5 from this reference. For the particles in each size bin, we compute the absolute magnitude H from the usual equation as a function of that size bin’s mean particle diameter d (in millimeters) and geometric albedo p (assumed to be 0.15 for generic near-Earth asteroids and to match the DRA value):

$$H = 5 \log_{10} \left(\frac{1329}{d 10^{-6} \sqrt{p}} \right). \quad (9)$$

Herein, from Equation (7), we have

$$d = 2^{\frac{1}{3}} \left(\frac{1}{d_{u_i}^3} + \frac{1}{d_{l_i}^3} \right)^{-\frac{1}{3}}. \quad (10)$$

Then we get the apparent magnitude V by

$$V = H + \frac{\partial V}{\partial \phi} \phi + 5 \log_{10}(r_{\text{SP}} r_{\text{PO}}). \quad (11)$$

Herein, the phase slope $\partial V / \partial \phi = 0.013 \text{ mag deg}^{-1}$ from Hergenrother et al. (2020), ϕ is the phase angle in degrees, and r_{SP} and r_{PO} are the Sun-to-particle and particle-to-observer distances in au, respectively. This phase function is reasonably

well behaved for Bennu particles in roughly the 2–20 mm diameter range over phase angles from roughly 70° to 120° . Applying this model over our entire 0.05–100 mm particle diameter range for our simulated ejecta and the whole range of phase angles LICIAcube sweeps through (42° – 120°) in addition to the more limited range of phase angles for HST observations (53° – 76°) is an acceptable extrapolation. The apparent magnitude per particle, V , is converted back to flux per particle, which is in turn multiplied by the number of particles in the volume of space within the current cube intersected by the currently considered pixel column. Summation, within each pixel, over all cubes of all particle size bins yields the total flux per pixel.

When the camera selected is the LICIAcube Explorer Imaging for Asteroid (LEIA) or LICIAcube Unit Key Explorer (LUKE; see Table 1), the image data array containing the flux from particles is registered and coadded with a separate image containing flux from the Didymos and Dimorphos body surfaces, rendered by members of the DART Investigation Team’s Proximity Imaging Working Group and posted on the DART SOC web page. The latter images are generated for the same time stamps with very nearly identical sets of SPICE kernels plus the current DRA shape models derived from radar and light-curve observations according to common methodology as described in Naidu et al. (2020). The images’ pixel values, $x \in [0, 255]$, are converted to flux $f(x)$ via

$$f(x) = \frac{1329}{r_{SD}^2} p \frac{x}{255}, \quad (12)$$

where r_{SD} is the Sun-to-Didymos distance in au. The pixel coordinates of the centers of Didymos and Dimorphos in each image of the bodies are read from the metadata recorded in a text file accompanying that image. This is used with the prior-output pixel coordinates of the centers of Didymos and Dimorphos in the image of flux from particles to compute any small rotation and rescaling necessary to exactly match the image plane–projected line of centers between the two flux maps prior to their being coadded.

Finally, images are both plotted as magnitude per pixel with various descriptive metadata overlaid and written out in Flexible Image Transport System (FITS) format containing flux per pixel for delivery to the DART SOC web page. This is done both with and without applying convolution with the appropriate camera point-spread function (PSF). For LEIA, a PSF was provided by LICIAcube science team members, but for LUKE, a lack of characterizing the PSF of the actual flight article prelaunch led us to assume a simple Gaussian PSF with an FWHM of 1 pixel. The PSF matching use of the F350LP filter on WFC3-UVIS on HST was generated by one of the coauthors using the software `TinyTIM` (Krist et al. 2011).

6. Results of Nominal and Off-nominal Parametric Study

Here we present a brief case study applying all of the preceding methodology to nominal and off-nominal scenarios spanning realistic ranges of total amount/mass of ejecta and ejecta cSFD slope. The former, the total mass of ejecta, is one of many relevant properties of the impact calculated according to crater scaling relations as discussed in Section 2.3.1, given input surface material strength, Y , and target body porosity. We interpolate across the various Housen & Holsapple (2011)

material cases to obtain values for the crater scaling relation parameters matching a target porosity of 35%. Didymos’s geometric albedo of $p = 0.15 \pm 0.04$ (Naidu et al. 2020) and S-class spectral type (de Leon et al. 2006) establish that the best meteorite analog for Didymos is L/LL chondrite (Dunn et al. 2013), for which typical grain densities are $3480 \pm 120 \text{ kg m}^{-3}$ (Flynn et al. 1999). Assuming the same composition between the two binary components, this grain density, together with the DRA bulk density of Dimorphos ($2200 \pm 350 \text{ kg m}^{-3}$), allows for 24%–49% porosity, so 35% porosity is a reasonable choice. The ejecta cSFD slope is unaddressed in the Housen & Holsapple (2011) work and may be chosen independent of total ejecta mass, keeping in mind the discussion immediately following Equation (1). Table 2 gives our nominal and off-nominal case names, along with their values of crater scaling relation parameters and inputs, calculated properties of the impact, and assumed cSFD power-law slope and particle size range.

Due to manuscript length limitations, we mostly highlight results from the nominal case, and even then, we are able to include relatively few of the simulated images here. Figure 5 shows simulated LEIA images for the nominal case, with the LEIA PSF applied, at four different epochs postimpact during the flyby. At first, including the image shown in Figure 5(a), the perspective is looking down the throat of the ejecta cone opening toward the observer. Ejecta first begin to pass out of the field of view (FOV) of LEIA by $t \approx 120$ s and fully fill the FOV by $t \approx 137$ s. Up until $t \approx 155$ s, including the image shown in Figure 5(a), the very fastest ejecta are sparsely distributed along the cone and isolated to subcubes of 3D space with intervening empty subcubes, leading to a pixelated appearance. LICIAcube flies through the geometric extension of the ejecta cone at $t \approx 156$ s, at which time the distance from LICIAcube to Dimorphos is $\Delta \approx 63$ km.

Thereafter, the perspective is looking at the ejecta cone from outside of it and from the side with a rapidly changing phase angle. The two images of Figures 5(b) and (c) are approximately equally separated in time from the epoch of closest approach at $t \approx 161$ s ($\Delta \approx 51$ km) but have a large shift in vantage point. In such images of the ejecta cone from the side, another artifact of the cube file methodology employed is apparent; some larger cubes of space do not get sufficiently subdivided to avoid spreading brightness outside of what we expect in reality to be a relatively sharply defined cone boundary. The cube files these images were generated from were made by setting $n_{bc} = 200$ (as in Equation (A1)), $N_{min} = 6$, and $maxlevel = 13$ (both as in Equation (A11)). We found that varying these parameters led to an unavoidable trade-off between greater sharpness of the ejecta cone in side aspect at closer distances but worse pixelation of the ejecta field at farther distances and the reverse. Mitigation of both issues together rather than in trade-off is planned for future work. Note that the minimum distance from LICIAcube to any ejecta passes through a minimum of only ≈ 42 km a little before the epoch of closest approach.

Still later in time, the perspective is looking back at the ejecta in forward scatter, as in Figure 5(d). Due to the relatively slow rate of ejecta cloud expansion, the ejecta once again lies entirely within the FOV by $t \approx 260$ s. The phase angle of the ejecta during the following receding phase of the flyby asymptotes toward 120° , so we do not expect to encounter the high phase angle/low scattering angle surge in the phase

Table 2

Case Names and Corresponding Values of Crater Scaling Relation Parameters and Inputs, Calculated Properties of the Impact, and Assumed cSFD Power-law Slope

Parameter/Quantity	Nominal	MinMassShallow	MinMassSteep	MaxMassShallow	MaxMassSteep
Net surface acceleration, g			$5.841532 \times 10^{-5} \text{ m s}^{-2}$		
DART effective radius, a			1.2407 m		
DART mass, m			536 kg		
DART impact speed, U			$6144.675 \text{ m s}^{-1}$		
DART mean density, δ			67.0 kg m^{-3}		
Target bulk density, ρ_B			$2202.055 \text{ kg m}^{-3}$		
Target porosity			35%		
Target cohesive strength, Y	100 Pa				10 Pa
Density scaling exponent, ν			0.4		
Velocity exponent, μ			0.41		
C_1			0.55		
k			0.3		
H_1			0.59		
H_2			0.39		
n_1			1.2		
n_2			1.0		
p			0.3		
Min. launch velocity, $V_{0\text{min}}$	$\approx 0 \text{ m s}^{-1}$		$\approx 0 \text{ m s}^{-1}$		$< 0.01 \text{ m s}^{-1}$
Max. launch velocity, $V_{0\text{max}}$	69.204 m s^{-1}		64.647 m s^{-1}		70.197 m s^{-1}
Final crater radius, R	13.000 m		5.058 m		20.843 m
Crater formation duration, T	103.71 s		4.03 s		525.80 s
Total ejecta mass, M_{tot}	$1.449 \times 10^6 \text{ kg}$		$8.329 \times 10^4 \text{ kg}$		$5.979 \times 10^6 \text{ kg}$
Ejecta particle size range			$0.05 \text{ mm} \leq d \leq 100 \text{ mm}$		
cSFD power-law slope	-2.3017	-2.0	-3.0	-2.0	-3.0

curve, which is not modeled through the simple linear phase slope of Equation (11) anyway. Incorporation of a more realistic phase curve including both geometric and diffraction effects is also planned for future work. Consistent with the departure geometry, the distances from observer to Dimorphos and observer to closest ejecta are nearly identical throughout this part of the flyby.

Several kinds of analysis should be applicable to the actual images from the LICIAcube vantage point, especially near closest approach, when the highest LEIA resolution on Dimorphos’s surface is achieved ($\approx 1.4 \text{ m}$). First, we should be able to measure the ejecta cone opening angle. Second, we should be able to estimate the ejecta cone center line/axis as a unit vector in 3D space through measuring its projection into the image plane across different times when the vantage point changes, but we are still generally looking at the cone from the side. This is important as a first guess for the direction of the net momentum carried by the ejecta, which, in combination with the surface normal at the impact point, determines ϵ within the β estimation approach outlined in Appendix B of Rivkin et al. (2021). We also intend to look for any large blocks or boulders within the ejecta cone, which, even if unresolved themselves, may introduce asymmetries in the cone close to the Dimorphos surface (cf. the “boulder shadowing effect” observed in Hayabusa2’s SCI experiment; Arakawa et al. 2020). Another route of analysis using optical depth profiles sliced through the ejecta cone as viewed from different camera positions is presented and discussed in Cheng et al. (2022).

Next, we show in Figure 6 some selected simulated HST/WFC3-UVIS images, also for the nominal case but from a very distant vantage point and after longer times postimpact. Note that, for efficiency, the cube files these images were generated from were made with slightly different settings of $n_{\text{bc}} = 100$, $N_{\text{min}} = 6$, and $\text{maxlevel} = 13$. Some pixelation of the ejecta cone is still apparent for early times due to the spatial sparsity

of the smaller population of the highest-velocity ejecta, but the plume becomes more uniformly represented at later times in its evolution. It is also interesting to note that as the ejecta cone becomes more diffuse over time, a distinct tail also emerges, growing toward the left side of the images. This is formed by the far more abundant population of low-velocity ejecta that has not progressed very far “up” the surface of the ejecta cone before getting swept by SRP out of a trajectory following the cone and antisunward. Note again that for these simulations, our minimum sampled particle size was $d = 0.05 \text{ mm}$. Assuming particles of that minimum size were to depart from Dimorphos directly antisunward (inconsistent with the actual ejecta cone geometry) and with an escape velocity from the binary system (at the distance of Dimorphos from Didymos) of $v_{\text{Sys}} \approx 0.24 \text{ m s}^{-1}$, the maximum distance antisunward that those particles can reach under acceleration by SRP can be calculated as a function of time. An antisunward vector of that length originating from Dimorphos and projected into the image plane can be compared against the furthest extent reached by such a tail within the planned actual images at any given time postimpact once the tail becomes discernible. This should allow us to constrain the actual smallest ejecta size relative to our cutoff size used in simulations. Put another way, because the acceleration of particles due to SRP is strongly dependent upon particle size, analysis of the length of such a tail versus time in actual images should allow us to constrain where the small-size rolloff in the cSFD is.

Note that, unlike for the LEIA and LUKE simulated images, for these simulated HST images, we do not coadd in the brightness of Didymos and Dimorphos themselves, which would entirely lie within the single central pixel (pixel scale at Dimorphos of $\approx 2 \text{ km}$ at the impact epoch). Nor do we add in any other point sources, such as background stars. In this sense, we are showing in the images the information content due to ejecta alone without any additional interference or obfuscation.

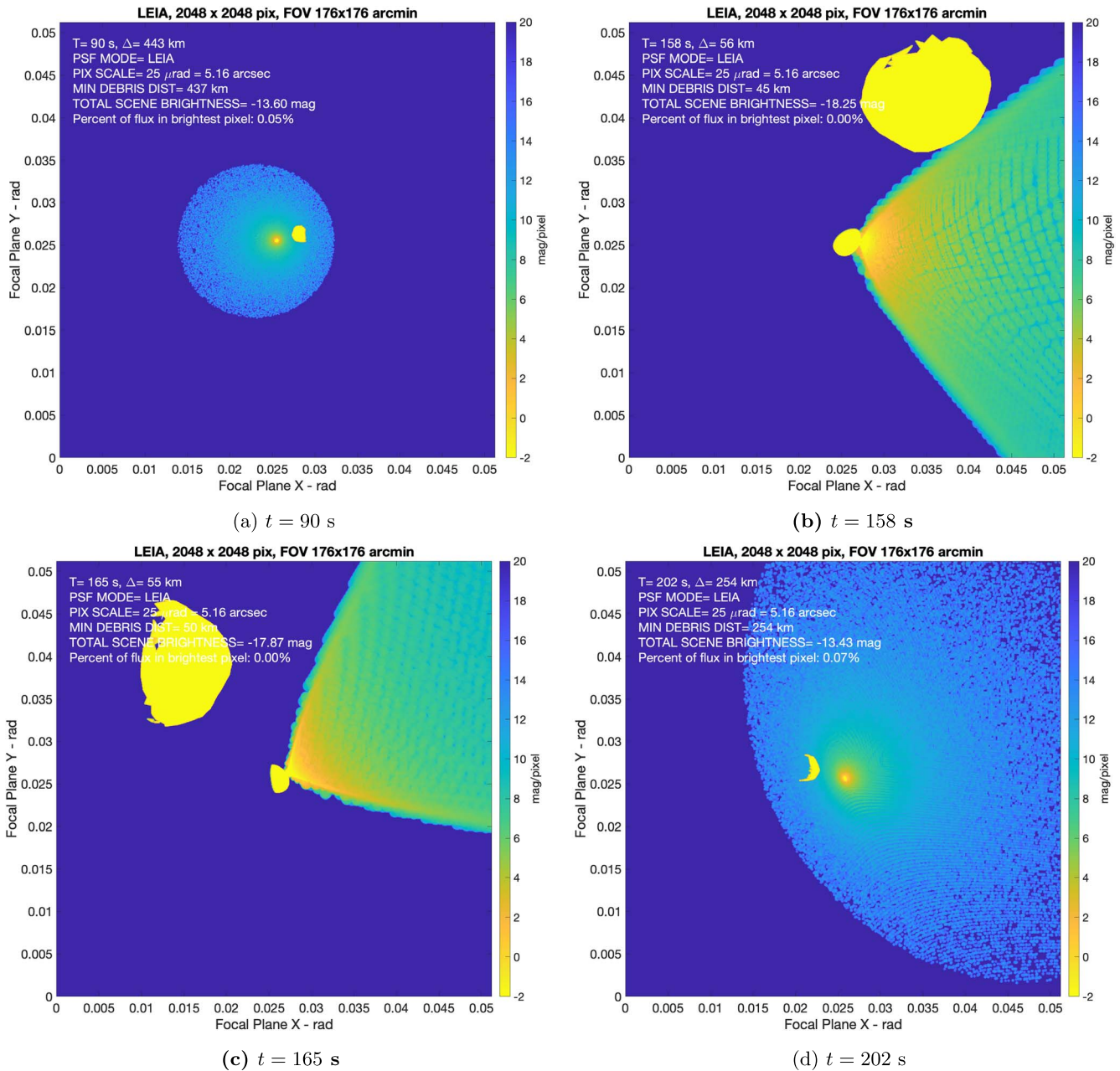


Figure 5. Simulated LEIA images for the nominal case, with LEIA PSF applied, at $t = 90, 158, 165,$ and 202 s ($t = 0$ at the time of impact). Note that the color scale indicates magnitude per pixel (magnitude herein means the usual astronomical magnitude as a measure of brightness) and remains fixed at $[-2, 20]$ for all frames. The distances from the camera to Dimorphos (Δ) are about 443, 56, 55, and 254 km. The minimum distances from LICIAcube to any ejecta are about 437, 45, 50, and 254 km.

This allows us to test our image analysis techniques in the most ideal and least conservative circumstances first. By similar reasoning, we first choose to apply those techniques to no-PSF images in what follows.

For further analysis of the simulated HST images, we seek to develop concise plots capturing their information content. Focusing on the innermost and brightest region of the images, we form an annulus out of all pixels within a certain range of pixel distance r from the target in the image plane. We then spatially average across all radii in the annulus and across small angular bins and plot the resulting mean magnitude per pixel against the single dimension of angle going around within the annulus. Combining traces for many concentric annuli yields figures such as those shown in Figure 7. The panels of Figure 7

are for times matching the images in Figure 6. One can clearly see the formation of the ejecta tail at $\approx 70^\circ$ in Figure 7(b). The characteristic two peaks, or “cat ears,” in each line of Figure 7(a) flatten out and broaden beyond the initial projection of the ejecta cone, i.e., spread out beyond just the upper right quadrant, by the time of Figure 7(b). Note that the integrated brightness under the curves for the same annulus increases from Figures 7(a) to 7(b), as brightness is moving out of the $r < 10$ central disk over time.

In Figure 8, we perform another level of spatial averaging, over all angles going around annuli, to get radial profiles of mean magnitude per pixel while introducing the time dimension through multiple lines. This tells an interesting story when put up against the summation of total ejecta

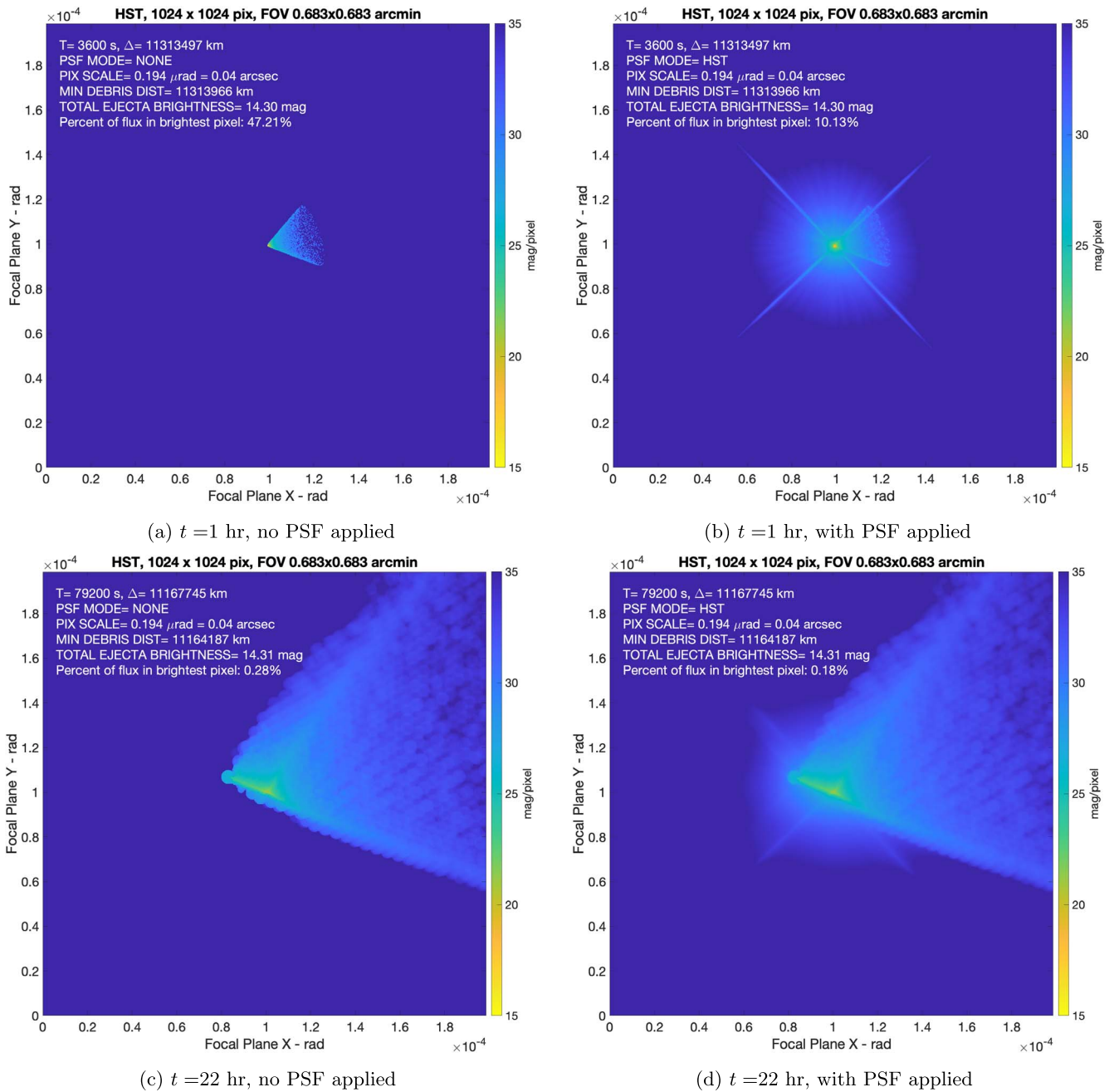
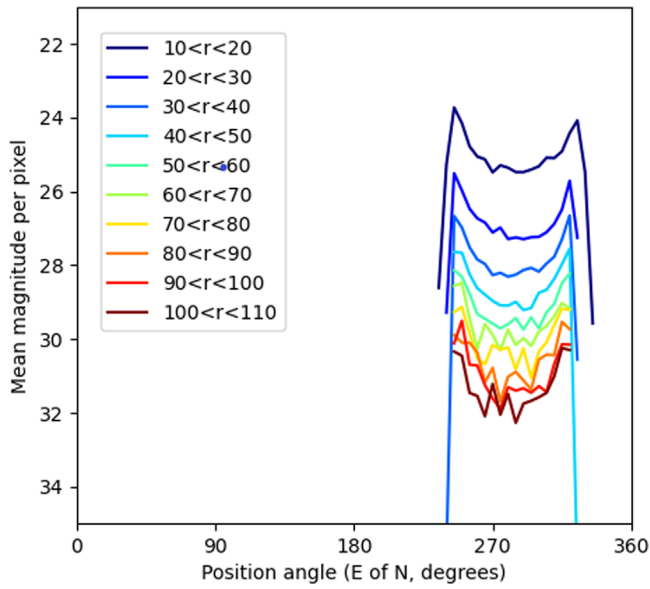


Figure 6. Simulated HST/WFC3-UVIS images for the nominal case, without (left) and with (right) the appropriate camera PSF applied, at $t = 1$ (top) and 22 (bottom) hr. Again, $t = 0$ at the time of impact. Note that the color scale indicates magnitude per pixel and remains fixed at [15, 35] for all frames. The total ejecta brightness integrated over the whole FOV remains nearly constant at 14.30–14.31 mag, but the percent of that brightness concentrated in the brightest pixel declines precipitously from 47.21% in panel (a) to 0.28% in panel (c) with no PSF applied and from 10.13% in panel (b) to 0.18% in panel (d) with PSF applied. See text for discussion of apparent structure.

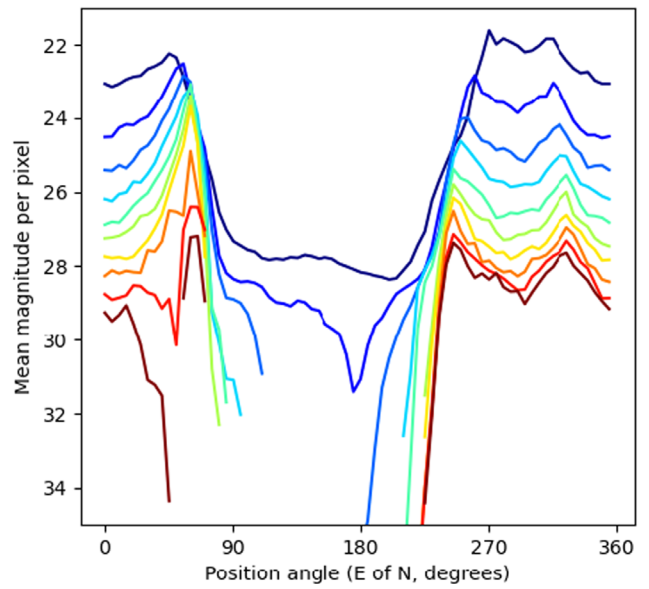
brightness over the whole FOV for each of the times having corresponding lines in Figure 8. Whether that calculation is made with no PSF applied or with the PSF applied, the only real difference is that the PSF spreads out brightness such that the percent of total flux in the image that is concentrated in the brightest pixel goes down in the with-PSF case. We still find that the total ejecta brightness within the FOV holds roughly constant over the whole of the first 48 hr postimpact (14.30 mag dropping to 14.31 mag). However, Figure 8 describes the time evolution of brightness only within the region between 10 and 110 pixels from the target. The brightness values in the annuli forming this region grow with time throughout the first

day as brightness moves out of the central disk with $r < 10$ and into and through those annuli. An outward-moving “wave” of brightness is apparent in the last ≈ 10 hr of the first day postimpact. Yet across the whole FOV, the total ejecta brightness is nearly conserved for all times up to $t = 48$ hr. This means that minimal brightness is being lost through the relatively small amount of fastest ejecta passing outside of the FOV up until ≈ 48 hr. That changes and the total ejecta brightness falls off steadily and significantly from days 2 through 20 postimpact.

Next, we seek to compare how these profiles differ between the nominal and off-nominal cases. This is shown for two

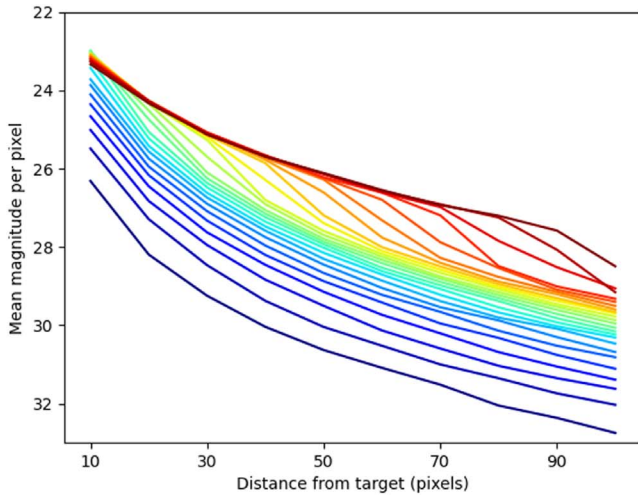


(a) $t=1$ hr, no PSF applied

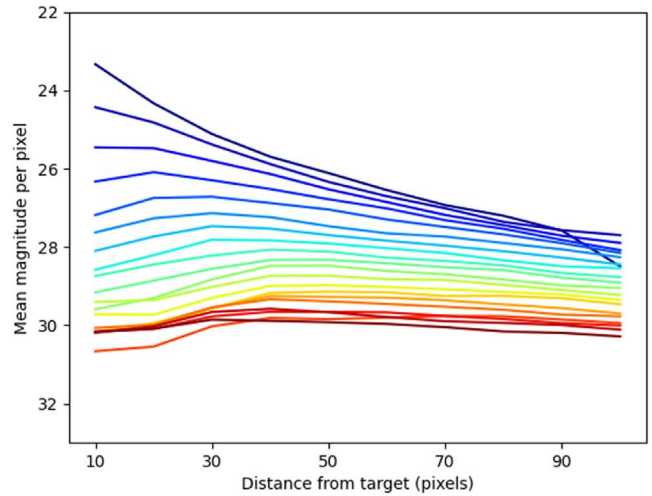


(b) $t=22$ hr, no PSF applied

Figure 7. Angular profiles of mean magnitude per pixel going from north toward east (i.e., counterclockwise from up) in the no-PSF-applied images of (a) Figure 6(a) and (b) Figure 6(c). Each line is for a different annulus formed by pixels within the range of pixel distance r from the target (Dimorphos) indicated by the legend. The horizontal axes are in degrees, and the angular bins averaged over are 5° wide.



(a) $1 \text{ hr} \leq t \leq 24 \text{ hr}$, no PSF applied



(b) $1 \text{ day} \leq t \leq 20 \text{ days}$, no PSF applied

Figure 8. Radial profiles of mean magnitude per pixel averaged within the annuli defined for Figure 7 over all angular positions going around each annulus. The horizontal axes are actually giving the pixel distance r from the target (Dimorphos) of the inner edge of the 10 pixel wide annuli. For panel (a), the lines are for 1 hr increments from $t = 1$ (darkest blue) to 24 (darkest red) hr, while for panel (b), the lines are for 1 day increments from $t = 24 \text{ hr} = 1 \text{ day}$ (darkest blue) to 20 days (darkest red).

selected times in Figure 9. It is apparent that our variation of input surface material strength by a factor of 1000, leading to a variation in the total mass of the ejecta by a factor of about 70, produces a change in the level of the profiles by about 3 mag pixel⁻¹ closest to the target, diminishing to less than 1 mag pixel⁻¹ at greater distances. In contrast, a change in the cSFD slope from -2.0 to -3.0 raises the profiles by about 4 mag pixel⁻¹ regardless of distance from the target. The change in the profile shape with the total mass of the ejecta versus a simple bias of the profile with the cSFD slope suggests that it may be possible to independently estimate the total mass of the ejecta and cSFD slope from such profiles from actual images. In Figure 9(b), we observe even

more crossing of the curves due to different profile shapes as a function of these two independent parameters. It appears that a greater relative abundance of smaller particles whose trajectories are more quickly modified by SRP will differentiate the appearance of time-varying features within such profiles. It is also planned to derive surface boulder/rock size–frequency distributions from the last and highest-resolution images taken by the Didymos Reconnaissance and Asteroid Camera for Optical navigation (Pajola et al. 2022). Extrapolating that to particles that are smaller by many orders of magnitude may also allow us to independently constrain the cSFD slope, leading to a separate determination of these two parameters of interest.

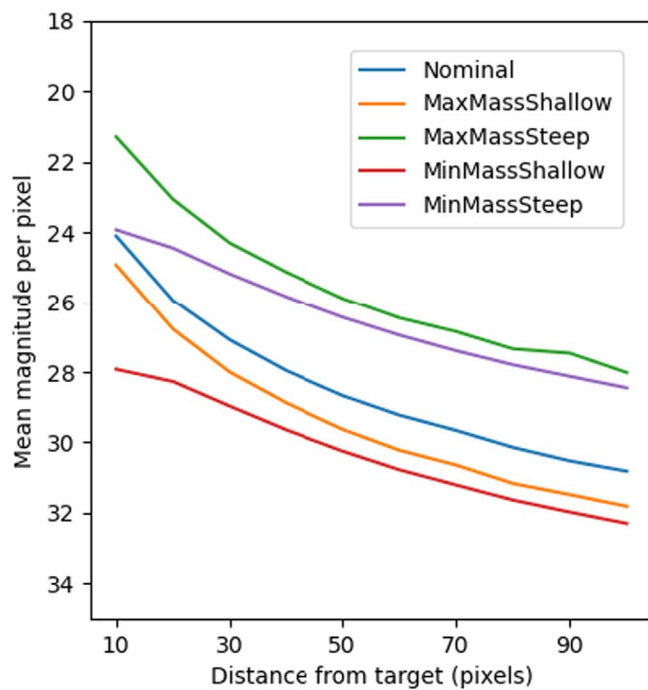
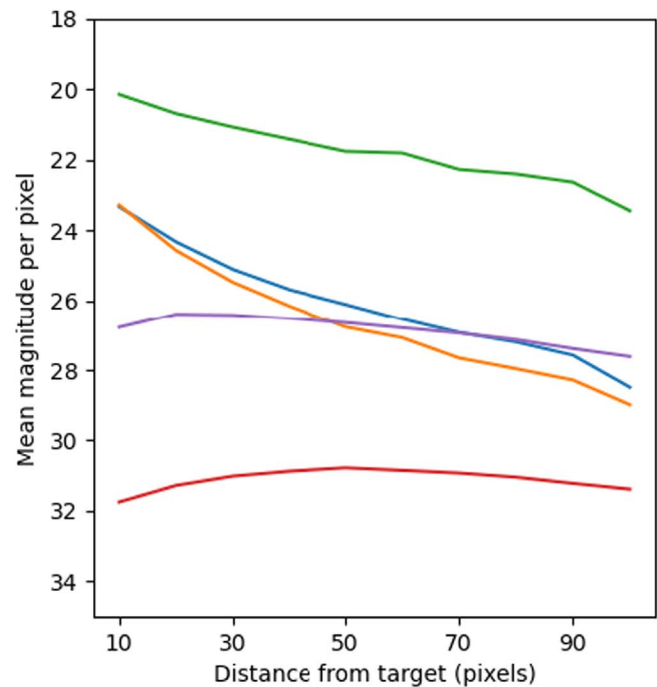
(a) $t=6$ hr, no PSF applied(b) $t=24$ hr, no PSF applied

Figure 9. Radial profiles of mean magnitude per pixel, created the same way as for Figure 8 but for two specific times plotted within Figure 8(a) and now comparing the nominal versus off-nominal cases having different total masses of ejecta and cSFD power-law slopes as specified in Table 2.

7. Conclusions

In this paper, we have presented various efforts within the DART Investigation Team’s Ejecta Working Group to predict the characteristics, quantity, dynamical behavior, and observability of DART impact ejecta. We have discussed various methodologies for simulation of the impact/cratering process with their advantages and drawbacks in relation to initializing ejecta for subsequent dynamical propagation through and away from the Didymos system. We have discussed the most relevant forces acting on ejecta once decoupled from the target surface and highlighted various software packages we have developed and used to dynamically simulate ejecta under the action of those forces. With the use of some additional software packages, we have explored the influence of additional perturbing effects, such as interparticle collisions within true N -body codes and nonspherical and rotating particles’ interplay with SRP. We have found that early-timescale and close-proximity ejecta evolution is highly sensitive to some of these effects (e.g., collisions coupled with particle shape can increase the rotational and kinetic energy of particles and change their velocity distribution up to a few tens of percent) while relatively insensitive to other factors (e.g., particle temperature). We have presented a methodology for turning the time-evolving size- and spatially discretized number density field from dynamical simulation of ejecta into simulated images from multiple platforms/cameras over wide-ranging vantage points and timescales. We have presented such simulated images for nominal and off-nominal cases along with preliminary image analysis foreshadowing the information content we may be able to extract from the actual images taken during and after the DART encounter.

Avenues for future work include, as mentioned earlier, (a) careful testing and implementation of the handoff procedure

based on velocity field in order to make ejecta initialization more realistic; (b) in the interface of ejecta dynamical simulation to synthetic image generation, simultaneous improvement of both the sharpness of definition of the ejecta cone in close proximity to Dimorphos and uniformity of the ejecta field at a greater distance from Dimorphos; and (c) incorporation of a more realistic phase curve including both geometric and diffraction effects and, ultimately, use of a proper radiative transfer code to handle multiple scattering as well. Ongoing development of image analysis applicable to the Earth-vicinity/HST vantage point images will also aim to accomplish proper estimation/inversion of the total ejecta mass and cSFD slope, if they can be disentangled by leveraging other DART encounter data sets. The total ejecta mass will, in turn, constrain the key target properties, such as cohesive strength and porosity. Full success in this domain would be to determine whether the impact is gravity- or strength-controlled even before the “ground truth” is provided by Hera’s later detailed characterization of the system.

This work was supported in part by the DART mission, NASA contract No. 80MSFC20D0004 to JHU/APL. Some of this work was carried out at the Jet Propulsion Laboratory, California Institute of Technology, under a contract with the National Aeronautics and Space Administration (80NM0018D0004). P.M., S.D.R., and Y.Z. acknowledge funding support from the European Union’s Horizon 2020 research and innovation program under grant agreement No. 870377 (project NEO-MAPP). P.M. acknowledges funding support from the French space agency CNES. F.F. acknowledges funding from the Swiss National Science Foundation (SNSF) Ambizione grant No. 193346. S.R.S. acknowledges support from the DART Participating Scientist Program, grant no. 80NSSC22K0318. A.R. and S.I. acknowledge financial support from the Agenzia Spaziale Italiana (ASI; contract

No. 2019-31-HH.0 CUP F84I190012600). A.C.B. acknowledges funding support from the European Union’s Horizon 2020 research and innovation program under grant agreement No. 870377 (project NEO-MAPP) and the Spanish MICINN RTI2018-099464-B-I00.

Appendix

Approach to Generation of Cube Files

A.1. Algorithm for Generating Cube File Records for Base Grid

At a given time postimpact, t , we obtain from the set of ejecta simulation output files for a previously completed simulation of N ejecta particles the positions and velocities of the N_t particles still in flight, meaning those particles with a launch time $t_0 < t$ and a final disposition time $t_f > t$. Here t_f is the time of reaching one of the tracked fates of return impact to secondary, transfer impact to primary, or escape from the system (if that is being tracked). These positions \mathbf{r} and velocities \mathbf{v} are coordinated in the user-specified frame (either International Celestial Reference Frame or Didymos heliocentric orbital radial–tangential–normal frame). We get initial guesses for cell edge length along each of the \hat{x} -, \hat{y} -, and \hat{z} -axes of the frame as follows:

$$l_i = \frac{\max |N_t(r_i) - \min |N_t(r_i)|}{n_{bc}}, \quad i \in \{x, y, z\}. \quad (\text{A1})$$

From these, we choose the smallest edge length as the edge length for the cubes of our base grid, i.e., $L = \min(l_x, l_y, l_z)$. Then the number of base grid divisions along each axis is given by

$$n_i = \text{ceil}\left(\frac{\max |N_t(r_i) - \min |N_t(r_i)|}{L}\right) + 1, \quad i \in \{x, y, z\}. \quad (\text{A2})$$

The origin \mathbf{r}_0 of the base grid is then placed at

$$\mathbf{r}_0 = \min |N_t(r_i) - \frac{L}{2}, \quad i \in \{x, y, z\}. \quad (\text{A3})$$

This ensures that all particles lie in the first octant of the base grid and will have positive integers for the base grid indices. The total number of cubes in the base grid = $n_x \times n_y \times n_z > n_{bc}^3$, with the cubes increasing in size as the whole ejecta field expands in 3D space over time. This will likely correspondingly require finer subdivision of the base cubes as time advances. The particle size bins under consideration are printed in the output cube file’s `ascii`

header. For each particle in flight, we identify the integer ID s of the size bin it falls in (starting counting from 1). Then the 3D base grid indices assigned to that particle are

$$\begin{bmatrix} i \\ j \\ k \end{bmatrix} = \text{floor}\left(\frac{\mathbf{r} - \mathbf{r}_0}{L}\right) + 1. \quad (\text{A4})$$

The nonempty base grid cells are then identified as the unique rows of the $N_t \times 4$ matrix formed by stacking up each row $[s, i, j, k]$. Of course, the number of nonempty cells in the full 4D (size bin, then spatial dimensions) grid will be greater than the number of nonempty cells in the 3D (spatial dimensions only) grid by construction.

Looping through each unique nonempty 4D base grid cell containing N_b propagated particles, we can calculate the propagated quantity of interest P_b and the full-scale population quantity of interest Q_b for that base grid cell as follows. Let \mathbf{x} be the length N_t logical vector whose elements are either 1, if the corresponding propagated particle is in the considered base grid cell, or zero. This is easily obtained in MATLAB by an array-to-row equality operation within a row-wise product across columns. Let \mathbf{u} be the length N_t vector of ones, let \mathbf{p} be the length N_t vector of particle multipliers, let \mathbf{m} be the length N_t vector of particle masses, and let \mathbf{v} be the length N_t vector of particle velocity magnitudes; i.e., each element of \mathbf{v} equals $\|\mathbf{v}\|$ for that particle. Then

$$N_b = \sum_{l=1}^{N_t} x_l = \mathbf{u} \cdot \mathbf{x}, \quad (\text{A5})$$

and Table 3 gives the quantities of interest. If N_b is less than some user-specified minimum, N_{\min} , then we just write an output file record as

$$[s, i, j, k, 0, 1, 1, 1, N_b, P_b, Q_b].$$

The first nine record elements are integers, and the last two record elements are single-precision float (if binary output) or printed in six postdecimal digit exponential format (if `ascii` output). This record can be interpreted as specifying that we have N_b, P_b, Q_b for particles in the s th size bin located within the cubic region of space having opposing corners at

$$\mathbf{r}_0 + L(i-1)\hat{x} + L(j-1)\hat{y} + L(k-1)\hat{z}, \quad (\text{A6})$$

$$\mathbf{r}_0 + L i \hat{x} + L j \hat{y} + L k \hat{z}. \quad (\text{A7})$$

The fifth element of the record is zero because we have performed zero levels of subdivision on this base grid cell; then, of course, the subdivision indices in the sixth through

Table 3
How to Compute Propagated and Full-scale Population Quantities of Interest

User-specified Quantity of Interest	Units	P_b	Q_b
Number density	No. m ⁻³	$(\mathbf{u} \cdot \mathbf{x})/L^3$	$(\mathbf{p} \cdot \mathbf{x})/L^3$
Mass density	kg m ⁻³	$((\mathbf{m} \cdot \mathbf{x})/L^3$	$((\mathbf{m}^* \mathbf{p}) \cdot \mathbf{x})/L^3$
Momentum density	(kg · m s ⁻¹) m ⁻³	$((\mathbf{m}^* \mathbf{v}) \cdot \mathbf{x})/L^3$	$((\mathbf{m}^* \mathbf{v} \mathbf{p}) \cdot \mathbf{x})/L^3$
Kinetic energy density	J m ⁻³	$\frac{1}{2}((\mathbf{m}^* \mathbf{v}^* \mathbf{v}) \cdot \mathbf{x})/L^3$	$\frac{1}{2}((\mathbf{m}^* \mathbf{v}^* \mathbf{v} \mathbf{p}) \cdot \mathbf{x})/L^3$
Number flux	No. m ⁻² day ⁻¹	$86,400(\mathbf{v} \cdot \mathbf{x})/L^3$	$86,400(\mathbf{v}^* \mathbf{p}) \cdot \mathbf{x})/L^3$
Mass flux	kg m ⁻² day ⁻¹	$86,400((\mathbf{m}^* \mathbf{v}) \cdot \mathbf{x})/L^3$	$86,400((\mathbf{m}^* \mathbf{v} \mathbf{p}) \cdot \mathbf{x})/L^3$
Momentum flux	(kg · m s ⁻¹) m ⁻² day ⁻¹	$86,400((\mathbf{m}^* \mathbf{v}^* \mathbf{v}) \cdot \mathbf{x})/L^3$	$86,400((\mathbf{m}^* \mathbf{v}^* \mathbf{v} \mathbf{p}) \cdot \mathbf{x})/L^3$
Kinetic energy flux	J m ⁻² day ⁻¹	$43,200((\mathbf{m}^* \mathbf{v}^* \mathbf{v}^* \mathbf{v}) \cdot \mathbf{x})/L^3$	$43,200((\mathbf{m}^* \mathbf{v}^* \mathbf{v}^* \mathbf{v} \mathbf{p}) \cdot \mathbf{x})/L^3$

Note. An asterisk means elementwise vector multiplication, and “flux” is taken to mean an omnidirectional cumulative total, so it is also a scalar.

eighth elements are just 1. If, on the other hand, $N_b \geq N_{\min}$, then we attempt subdivision of this base grid cell, which will handle calculation and writing of records for successive subcells.

A.2. Algorithm for Generating Cube File Records for Subdivisions of Base Grid

If we are going to attempt subdivision, we make a first call on a function that recursively calls itself as needed. The documentation block for this function is simply as follows:

```
function recursive_subdivision(writeout,
fiddy, baseInd, level, bisecthistUp, qtyUp,
LUp, CornerUp, np, rp, intermed1, intermed2,
nsamp, threshold, maxlevel, debug).
```

1. `writeout` = [static] flag controlling whether to write out to file in `ascii` or `binary`.
2. `fiddy` = [static] file identifier for output file to write to.
3. `baseInd` = [static] indices of the base cube that the current cube lies within (note that the current cube may be the same as the base cube), 1×4 integer.
4. `level` = number of levels of subdivision of the base cube that we are trying out during the current entry into this function, positive integer, i.e., 1, 2, 3, ...
5. `bisecthistUp` = three-row array, each column of which records the history of successive bisections through which we arrive in the current cube.
6. `qtyUp` = value for the quantity of interest computed across the whole of the current cube.
7. `LUp` = edge length of the current cube, km.
8. `CornerUp` = 3×1 , coordinates of the minimum (along each axis) corner of the current cube with regard to the chosen global frame's origin, km.
9. `np` = number of actually propagated particles within the current cube, integer.
10. `rp` = $np \times 3$, position coordinates of actually propagated particles within the current cube with regard to the chosen global frame's origin, m.
11. `intermed1` = $1 \times np$, intermediate quantity, without multiplying by particle multipliers, for those actually propagated particles within the current cube.
12. `intermed2` = $1 \times np$, intermediate quantity, including multiplying by particle multipliers, for those actually propagated particles within the current cube.
13. `nsamp` = [static] minimum number of actually propagated particles in a nonempty cell, below which we do not attempt another level of subdivision, integer.
14. `threshold` = [static] minimum fraction by which the quantity of interest should vary between nonempty cells, at or below which we do not attempt another level of subdivision.
15. `maxlevel` = [static] maximum number of levels of subdivision allowed.
16. `debug` = [static] flag to turn on debugging printout.

Arguments marked with [static] will not change in value but instead persist through any chain of recursive calls on this function. The above should already give an idea of what is going on, but we will step through the logic next. Any chain of recursive calls on this function begins with passing 1 in as argument `level` and $[0, 0, 0]^T$ in as argument `bisecthistUp`, because the current cube starts off being the same as the spatial base cube, we are attempting a first level

of subdivision of it, and no bisection has occurred yet along any of the three coordinate axes. The first step is to set a new L equal to half the value passed in `LUp`. Returning to our previous notation, `np` passes N_b (at least for this first call), `nsamp` passes N_{\min} (always, consistently), `CornerUp` passes a new \mathbf{r}_0 for the current cube, and each row of `rp` passes the unchanged or global \mathbf{r} for one of the actually propagated particles within the current cube. In what follows, we may ignore some details of making units the same and matching MATLAB array dimensions. Using

$$\begin{bmatrix} i' \\ j' \\ k' \end{bmatrix} = \text{floor}\left(\frac{\mathbf{r} - \mathbf{r}_0}{L}\right) \quad (\text{A8})$$

gives a three-vector valued strictly zero or 1. The $N_b \times 3$ matrix formed by stacking up each row $[i', j', k']$ has a number of unique rows q strictly between one and eight. Here q gives the number of nonempty subcubes, and, looping over each of the nonempty subcubes, we do the following.

1. Append the currently considered unique row of the indices matrix onto the bisection history passed into this function by argument `bisecthistUp` as a new column on the right. That is,

$$\text{bisecthist} = \left[\text{bisecthistUp}, \begin{bmatrix} i' \\ j' \\ k' \end{bmatrix} \right]. \quad (\text{A9})$$

2. Calculate new \mathbf{x} as the length N_b logical vector of either 1, if the corresponding propagated particle is in the considered nonempty subcube, or zero. This is done using an array-to-row equality operation within a row-wise product across columns, similar to before.
3. Argument `intermed1` passed in new \mathbf{u} as length N_b vector of ones, while argument `intermed2` passed in new \mathbf{p} as length N_b vector of particle multipliers, so compute P_{sub} and Q_{sub} according to Table 3. If the user-specified quantity of interest is one of the seven other options besides number density, we simply pass through `intermed1` and `intermed2` the full product within the innermost parentheses in the P_b and Q_b columns of Table 3, instead of just ones vector \mathbf{u} or particle multipliers vector \mathbf{p} .
4. We have, similar to Equation (A5), the new sum of the new logical vector \mathbf{x} as

$$N_{\text{sub}} = \sum_{l=1}^{N_b} x_l = \mathbf{u} \cdot \mathbf{x}. \quad (\text{A10})$$

5. If we do not meet the logical union of these three conditions, where `threshold` earlier passed in the value f_{\min} ,

$$N_{\text{sub}} \geq N_{\min}, \quad \left| \frac{Q_{\text{sub}} - Q_b}{Q_b} \right| > f_{\min}, \quad \text{level} < \text{maxlevel}, \quad (\text{A11})$$

then we will write an output file record for the current nonempty subcube. This happens most often when N_{sub} shrinks to be less than N_{\min} , although the limitation to `maxlevel` levels of subdivision is there out of necessity

as a safety check. The record written looks like

$$[s, i, j, k, \text{level}, i_{\text{sub}}, j_{\text{sub}}, k_{\text{sub}}, N_{\text{sub}}, P_{\text{sub}}, Q_{\text{sub}}],$$

with the same formatting as before. Here the subcube indices $\{i_{\text{sub}}, j_{\text{sub}}, k_{\text{sub}}\}$ are dependent on the level of subdivision that has been carried out, or the value of `level`, and are calculated from each row of the new `bisecthist` matrix. This matrix essentially contains a history of successive (from leftmost column to rightmost column) spatial domain bisection outcomes on each of the three axes, valid for all of the particles in the currently considered subcube. The key is to treat each row of the matrix as a binary string to be converted to an integer. In particular, if $n = 1 + \text{level}$ is the number of columns in `bisecthist`, then

$$\begin{bmatrix} i_{\text{sub}} \\ j_{\text{sub}} \\ k_{\text{sub}} \end{bmatrix} = \begin{bmatrix} 1 \\ 1 \\ 1 \end{bmatrix} + \sum_{m=1}^n 2^{n-m} \text{bisecthist}(:, m). \quad (\text{A12})$$

6. If, on the other hand, we do meet the logical union of the conditions of Equation (A11), then we should attempt further subdivision. We call `recursive_subdivision` again, this time passing for the nonstatic arguments (in order) the value of `level` incremented by 1, the new `bisecthist`, Q_{sub} , the new L , the new global corner coordinates given by $\mathbf{r}_0 + L \text{bisecthist}(:, n)$, N_{sub} , the down-selection of \mathbf{r} from $N_b \times 3$ to $N_{\text{sub}} \times 3$ using new logical vector \mathbf{x} as indices, and the similar down-selection of \mathbf{u} quantity and \mathbf{p} quantity from $1 \times N_b$ to $1 \times N_{\text{sub}}$ using new logical vector \mathbf{x} as indices.

As a final note, records written out from within the recursive function can be interpreted as specifying that we have N_{sub} , P_{sub} , Q_{sub} for particles in the s th size bin located within the cubic region of space having opposing corners at

$$\begin{aligned} \mathbf{r}_0 + & \left[L(i-1) + \frac{L}{2^{\text{level}}}(i_{\text{sub}} - 1) \right] \hat{\mathbf{x}} \\ & + \left[L(j-1) + \frac{L}{2^{\text{level}}}(j_{\text{sub}} - 1) \right] \hat{\mathbf{y}} \\ & + \left[L(k-1) + \frac{L}{2^{\text{level}}}(k_{\text{sub}} - 1) \right] \hat{\mathbf{z}}, \end{aligned} \quad (\text{A13})$$

$$\begin{aligned} \mathbf{r}_0 + & \left[L(i-1) + \frac{L}{2^{\text{level}}} i_{\text{sub}} \right] \hat{\mathbf{x}} \\ & + \left[L(j-1) + \frac{L}{2^{\text{level}}} j_{\text{sub}} \right] \hat{\mathbf{y}} \\ & + \left[L(k-1) + \frac{L}{2^{\text{level}}} k_{\text{sub}} \right] \hat{\mathbf{z}}. \end{aligned} \quad (\text{A14})$$

Here \mathbf{r}_0 is the top-level or global origin of the base grid, and L is the original, undivided base cube edge length. One can easily verify that Equations (A13) and (A14) recover Equations (A6) and (A7) for base cube records and are thus sufficient for reading all records.

ORCID iDs

Andrew F. Cheng  <https://orcid.org/0000-0001-5375-4250>
 Stavro Ivanovski  <https://orcid.org/0000-0002-8068-7695>
 Patrick Michel  <https://orcid.org/0000-0002-0884-1993>
 Sabina D. Raducan  <https://orcid.org/0000-0002-7478-0148>
 Alessandro Rossi  <https://orcid.org/0000-0001-9311-2869>

Steven Chesley  <https://orcid.org/0000-0003-3240-6497>
 Elisabetta Dotto  <https://orcid.org/0000-0002-9335-1656>
 Fabio Ferrari  <https://orcid.org/0000-0001-7537-4996>
 Ludmilla Kolokolova  <https://orcid.org/0000-0002-9321-3202>
 Emily Kramer  <https://orcid.org/0000-0003-0457-2519>
 Jian-Yang Li  <https://orcid.org/0000-0003-3841-9977>
 Stephen R. Schwartz  <https://orcid.org/0000-0001-5475-9379>
 Stefania Soldini  <https://orcid.org/0000-0003-3121-3845>
 Gonzalo Tancredi  <https://orcid.org/0000-0002-4943-8623>
 Adriano Campo Bagatin  <https://orcid.org/0000-0001-9840-2216>
 Yun Zhang  <https://orcid.org/0000-0003-4045-9046>

References

- Acton, C., Bachman, N., Semenov, B., & Wright, E. 2018, *P&SS*, 150, 9
 Anderson, J. L. B., Schultz, P. H., & Heineck, J. T. 2003, *JGRE*, 108, 5094
 Arakawa, M., Saiki, T., Wada, K., et al. 2020, *Sci*, 368, 67
 Ballouz, R.-L., Richardson, D. C., Michel, P., & Schwartz, S. R. 2014, *ApJ*, 789, 158
 Ballouz, R.-L., Walsh, K. J., Richardson, D. C., & Michel, P. 2019, *MNRAS*, 485, 697
 Buhl, E., Sommer, F., Poelchau, M. H., Dresen, G., & Kenkmann, T. 2014, *Icar*, 237, 131
 Cheng, A. F., Michel, P., Jutzi, M., et al. 2016, *P&SS*, 121, 27
 Cheng, A. F., Raducan, S. D., Fahnestock, E. G., et al. 2022, *PSJ*, 3, 131
 Cheng, A. F., Rivkin, A. S., Michel, P., et al. 2018, *P&SS*, 157, 104
 Cheng, A. F., Stickle, A. M., Fahnestock, E. G., et al. 2020, *Icar*, 352, 113989
 Cintala, M. J., Berthoud, L., & Hörz, F. 1999, *M&PS*, 34, 605
 Daly, R. T., Ernst, C. M., Barnouin, O. S., et al. 2022, *PSJ*, in press
 Davis, A. B., & Scheeres, D. J. 2020, *Icar*, 341, 113439
 de Leon, J., Licandro, J., Duffard, R., & Serra-Ricart, M. 2006, *AdSpR*, 37, 178
 Dotto, E., Della Corte, V., Amoroso, M., et al. 2021, *P&SS*, 199, 105185
 Dunn, T. L., Burbine, T. H., Bottke, W. F., Jr., & Clark, J. P. 2013, *Icar*, 222, 273
 Everhart, E. 1985, in *An Efficient Integrator that Uses Gauss-Radau Spacings*, Astrophysics and Space Science Library, Vol. 115, ed. A. Carusi & G. B. Valsecchi (Dordrecht: Springer), 185
 Fahnestock, E., & Chesley, S. 2022, figshare doi:10.6084/m9.figshare.20044112
 Fehlberg, E. 1968, *Classical Fifth-, Sixth-, Seventh-, and Eighth-Order Runge-Kutta Formulas with Step-size Control*, NASA-TR-R-287, NASA, <https://ntrs.nasa.gov/citations/19680027281>
 Ferrari, F., Lavagna, M., & Blazquez, E. 2020, *MNRAS*, 492, 749
 Ferrari, F., Raducan, S., Jutzi, M., et al. 2021, in 7th IAA Planetary Defense Conf., Vienna, <https://trs.jpl.nasa.gov/bitstream/handle/2014/54868/CL%2321-1728.pdf?sequence=1>
 Ferrari, F., Tasora, A., Masarati, P., & Lavagna, M. 2017, *Multibody System Dynamics*, 39, 3
 Flynn, G. J., Moore, L. B., & Klöck, W. 1999, *Icar*, 142, 97
 Gault, D., Shoemaker, E., Moore, H., et al. 1963, *Spray Ejected from the Lunar Surface by Meteoroid Impact*, NASA-TN-D-1767, NASA, <https://ntrs.nasa.gov/citations/19630004711>
 Hergenrother, C. W., Maleszewski, C., Li, J. Y., et al. 2020, *JGRE*, 125, e06381
 Hermalyn, B., & Schultz, P. H. 2011, *Icar*, 216, 269
 Housen, K. R. 1992, *LPSC*, 23, 555
 Housen, K. R., & Holsapple, K. A. 2003, *Icar*, 163, 102
 Housen, K. R., & Holsapple, K. A. 2011, *Icar*, 211, 856
 Ivanovski, S. L., Lucchetti, A., Zanotti, G., et al. 2022, *PSJ*, submitted
 Johnson, B., Bowling, J. T., & Melosh, J. 2014, *Icar*, 238, 13
 Jutzi, M., & Michel, P. 2014, *Icar*, 229, 247
 Jutzi, M., Michel, P., & Richardson, D. C. 2019, *Icar*, 317, 215
 Kieffer, S. W. 1977, *JGR*, 82, 2895
 Krist, J. E., Hook, R. N., & Stoehr, F. 2011, *Proc. SPIE*, 8127, 81270J
 Luther, R., Zhu, M.-H., Collins, G., & Wünnemann, K. 2018, *M&PS*, 53, 1705
 Mazrouei, S., Daly, M. G., Barnouin, O. S., Ernst, C. M., & DeSouza, I. 2014, *Icar*, 229, 181
 Michel, P., Cheng, A., Küppers, M., et al. 2016, *AdSpR*, 57, 2529

- Michel, P., Kueppers, M., Sierks, H., et al. 2018, *AdSpR*, **62**, 2261
- Michel, P., Küppers, M., Campo Bagatin, A., et al. 2022, *PSJ*, **3**, 160
- Milani, A., Nobili, A., & Farinella, P. 1987, *Non-gravitational Perturbations and Satellite Geodesy* (Boca Raton, FL: CRC Press)
- Moreno, F., Campo Bagatin, A., Tancredi, G., Liu, P., & Domínguez, B. 2022, *MNRAS*, **515**, 2178
- Murray, C., & Dermott, S. 2000, *Solar System Dynamics* (Cambridge: Cambridge Univ. Press)
- Naidu, S. P., Benner, L. A. M., Brozovic, M., et al. 2020, *Icar*, **348**, 113777
- Naidu, S. P., Chesley, S. R., Farnocchia, D., et al. 2022, *PSJ*, submitted
- Nakamura, E., Makishima, A., Moriguti, T., et al. 2012, *PNAS*, **109**, E624
- Ormö, J., Raducan, S. D., Jutzi, M., et al. 2022, *E&PSL*, **594**, 117713
- Pajola, M., Barnouin, O. S., Lucchetti, A., et al. 2022, *PSJ*, in press
- Pravec, P., Thomas, C. A., Rivkin, A. S., et al. 2022, *PSJ*, **3**, 175
- Prieur, N. C., Rolf, T., Luther, R., et al. 2017, *JGRE*, **122**, 1704
- Raducan, S. D., Davison, T. M., & Collins, G. S. 2022, *Icar*, **374**, 114793
- Raducan, S. D., Davison, T. M., Luther, R., & Collins, G. S. 2019, *Icar*, **329**, 282
- Rainey, E. S. G., Stickle, A. M., Cheng, A. F., et al. 2020, *IIE*, **142**, 103528
- Richardson, D. C., Agrusa, H. F., Barbee, B., et al. 2022, *PSJ*, **3**, 157
- Richardson, D. C., Quinn, T., Stadel, J., & Lake, G. 2000, *Icar*, **143**, 45
- Rivkin, A. S., Chabot, N. L., Stickle, A. M., et al. 2021, *PSJ*, **2**, 173
- Rossi, A., & Fulchignoni, M. 2007, *AdSpR*, **40**, 173
- Rossi, A., Marzari, F., Brucato, J. R., et al. 2022, *PSJ*, **3**, 118
- Rossi, A., Marzari, F., & Farinella, P. 1999, *EP&S*, **51**, 1173
- Saiki, T., Imamura, H., Arakawa, M., et al. 2017, *SSRv*, **208**, 165
- Scheirich, P., & Pravec, P. 2022, *PSJ*, **3**, 163
- Schwartz, S. R., Michel, P., Jutzi, M., et al. 2018, *NatAs*, **2**, 379
- Schwartz, S. R., Richardson, D. C., & Michel, P. 2012, *Granular Matter*, **14**, 363
- Schwartz, S. R., Yu, Y., Michel, P., & Jutzi, M. 2016, *AdSpR*, **57**, 1832
- Soldini, S., Saiki, T., Ikeda, H., et al. 2020a, *P&SS*, **180**, 104740
- Soldini, S., Takeuchi, H., Taniguchi, S., et al. 2020c, *AsDyn*, **4**, 265
- Soldini, S., Yamaguchi, T., Tsuda, Y., Saiki, T., & Nakazawa, S. 2020b, *SSRv*, **216**, 108
- Stadel, J. G. 2001, PhD thesis, Univ. Washington
- Stickle, A. M., Burger, C., Caldwell, W. K., et al. 2022, *PSJ*, submitted
- Stickle, A. M., Rainey, E. S. G., Syal, M. B., et al. 2017, *Procedia Engineering*, **204**, 116
- Tancredi, G., Roland, S., & Bruzzone, S. 2015, *Icar*, **247**, 279
- Vallado, D. A. 2013, in *Fundamentals of Astrodynamics and Applications*, Space Technology Library, ed. J. Wertz (4th ed.; Hawthorne, CA: Microcosm Press)
- Walsh, K. J., & Jacobson, S. A. 2015, in *Asteroids IV*, ed. W. F. Bottke, F. E. DeMeo, & P. Michel (Tucson, AZ: Univ. Arizona Press), 375
- Watanabe, S., Hirabayashi, M., Hirata, N., et al. 2019, *Sci*, **364**, 268
- Werner, R. A., & Scheeres, D. J. 1997, *CeMDA*, **65**, 313
- Yu, Y., & Michel, P. 2018, *Icar*, **312**, 128
- Yu, Y., Michel, P., Schwartz, S. R., Naidu, S. P., & Benner, L. A. M. 2017, *Icar*, **282**, 313
- Zhang, Y., Jutzi, M., Michel, P., Raducan, S. D., & Arakawa, M. 2021a, *LPSC*, **52**, 1974
- Zhang, Y., Jutzi, M., Michel, P., Raducan, S. D., & Arakawa, M. 2021b, *EPSC 2021*, **EPSC2021-704**
- Zhang, Y., Richardson, D. C., Barnouin, O. S., et al. 2018, *ApJ*, **857**, 15
- Zhang, Y., Richardson, D. C., Barnouin, O. S., et al. 2017, *Icar*, **294**, 98